https://doi.org/10.5194/essd-2025-475
Preprint. Discussion started: 19 August 2025

Open Access Earth System Science Data Discussions

1 km annual forest cover and plant functional types dataset for China from 1980 to 2023

Bo Liu [1], Boyan Li [1], Fulai Feng [1], Yangcan Bao [1], Jing Li [1], Qi Feng [1,2]

[1]School of Geography and Tourism, Shaanxi Normal University, Xi'an, 710119, PR China
[2]Key Laboratory of Ecohydrology of Inland River Basin/Gansu Qilian Mountains Eco-Environment Research Center, Northwest Institute of Eco-Environment and Resources, Chinese Academy of Sciences, Lanzhou, 730000, PR China

Correspondence to: Boyan Li (byli@snnu.edu.cn) Qi Feng (qifeng@lzb.ac.cn)

Abstract. High–spatial–resolution and long-term data on forest cover and plant functional types (PFTs) are crucial for elucidating the impacts of forest cover change on the national terrestrial carbon balance. Since the 1980s, China has undergone a substantial expansion in its forest area, primarily driven by large-scale national afforestation programmes. However, existing land cover products have often failed to capture this long-term increasing trend, leading to an underestimation of forest cover change–related ecological processes. Here, we developed a high-resolution (1 km), annual forest cover dataset for China during 1980–2023. This dataset integrates spatial constraints from multi-source remote sensing data with provincial-level statistics from China's national forest inventories (NFIs), providing a consistent and spatially explicit record of forest dynamics over four decades. Building on this primary dataset, we further produced an annual PFT dataset that disaggregates total forest cover into eight distinct functional types, tailored for use in dynamic global vegetation models (DGVMs). Validation against independent data confirms the dataset's ability to accurately represent historical forest recovery, achieving an overall accuracy (OA) of 95.3 ± 0.5%, with classification accuracies for needleleaf and broadleaf forests ranging from 84.4% to 92.0%. To evaluate its applicability, we implemented the dataset within the Lund–Potsdam–Jena General Ecosystem Simulator (LPJ–GUESS). Compared to the widely used PFT dataset from the European Space Agency's Land Cover Climate Change Initiative (ESA CCI), our product yields a markedly improved simulation of key biophysical and biogeochemical processes in China, enhancing the accuracy of evapotranspiration, leaf area index (LAI), and vegetation carbon flux by 49.4%–77%. With its high spatial resolution, long–term temporal coverage, and detailed forest-type classification, our dataset offers a robust foundation for assessing the ecological impacts of forest restoration and for constraining estimates of China's forest carbon sink since 1980. The dataset is freely available at 10.5281/zenodo.16208012 (Liu et al., 2025).

1 Introduction

Large-scale afforestation programmes were implemented in China during the past four decades (Tong et al., 2018; Chen et al., 2019). As a result, forest area in China increased to around 230 million hectares, a rise of 85% compared to the early 1980s (IDS, 2018). Recent satellite observations revealed widespread "vegetation greening patterns" in China due to several large-scale conservation programmes (Piao et al., 2020). These changes have significant implications for carbon dynamics and

https://doi.org/10.5194/essd-2025-475
Preprint. Discussion started: 19 August 2025

ecosystem services. Specifically, they have enhanced carbon sequestration, reduced soil erosion and acidification in northern China, and altered regional climate patterns through changes in surface albedo, evapotranspiration (ET), and aerodynamic roughness (Liu et al., 2017; Hong et al., 2020). These findings underscore the critical role of afforestation in mitigating climate change and improving ecosystem stability at regional and global scales (Alkama and Cescatti, 2016; Yang et al., 2024).

Despite these positive developments, precisely quantifying the contribution of these land cover changes to the global carbon balance remains a significant challenge (Li et al., 2025; Yu et al., 2024). During the period 2014–2023, the net carbon emissions from the global land use, land use change, and forestry (LULUCF) sector were estimated at 4.1±2.6 Gt CO_2 yr^{-1}, accounting for 10% of total anthropogenic CO_2 emissions (Friedlingstein et al., 2024). The uncertainty of this estimate exceeds 50% of the mean flux, making LULUCF the most uncertain component in the global carbon budget (Friedlingstein et al., 2024; O'sullivan et al., 2022). These uncertainties primarily arise from disparities in model process representation, inconsistencies in flux definitions, variability in management practices, and spatiotemporal estimation differences in forest cover and its change rates (Ruehr et al., 2023; Hartung et al., 2021; Yu et al., 2022).

Although remote sensing has greatly improved the availability of land use and land cover change (LUCC) data, significant discrepancies among different datasets regarding the estimation of China's forest area propagates large uncertainties into modelling (Tu et al., 2024; Zhu et al., 2025); for instance, it has led to three to five-fold differences in estimates of China's terrestrial carbon storage from bookkeeping models (e.g., 17–33 Pg C vs. 6.18 Pg C) (Houghton and Hackler, 2003; Ge et al., 2008). Cross-dataset comparisons highlight the scale of this issue: estimates of China's forest area for the year 2010 from five different forest datasets ranged from 1.74 to 2.27 million km^2, a relative difference of 29% (Qin et al., 2015). Peng et al. (2024b) compared eight LULC datasets for the year 2020 and found a maximum discrepancy of 0.34 million km^2, an amount equivalent to 15% of the area reported by the national forest inventory (NFI). This inter-product inconsistency is particularly problematic as it contradicts the well-documented trend of forest expansion in China. According to NFI data, the nation's forest area more than doubled from 1.15 million km^2 in 1981 to 2.31 million km^2 by 2021 (IDS, 2018). This trend is consistent with broader assessments by the Food and Agriculture Organization of the United Nations (FAO), which attribute the shift in Asia's forest balance from a net loss in 1990–2000 to a marked net gain in 2000–2010 primarily to China's sustained afforestation efforts (FAO, 2016). However, long-term satellite-based LULC products have struggled to reproduce this marked increase (Yang and Huang, 2021). For example, the GlobeLand 30 product shows only a minor expansion of 5,700 km^2 between 2000 and 2020 (Chen et al., 2015), while the national land cover database of China (NLCD–China) even indicates a net loss of 14,000 km^2 from 2001 to 2015 (Wei et al., 2024). Consequently, due to these profound disagreements among datasets, the contribution of the LULUCF sector to China's regional carbon budget remains poorly constrained (Xia et al., 2023; Yu et al., 2022).

The NFI is considered the foundational national dataset for quantifying forest cover and biomass stocks (Zeng et al., 2015; Xia et al., 2023). Since the implementation of the second NFI during 1977–1981, a standardized sampling and survey methodology has been applied nationwide. Subsequently, eight further NFI campaigns have been conducted on a continuous five-year cycle (IDS, 2018). Owing to its extensive sample size covering the entire country, the forest area statistics provided by the NFI are widely regarded as a reference dataset. This large-scale inventory provides unique bottom-up information that

https://doi.org/10.5194/essd-2025-475
Preprint. Discussion started: 19 August 2025

complements top-down data from satellite remote sensing products, ensuring that the spatiotemporal dynamics of land use activities are captured. Indeed, previous studies have utilized the NFI dataset to estimate the national forest carbon budget (Fang et al., 2001; Piao et al., 2009). However, a key limitation of the NFI is that it only provides forest area statistics at the coarse provincial level. This spatial aggregation constrains its direct application for simulating carbon dynamics in spatially explicit earth system models (Zhu et al., 2025).

At both global and national scales, dynamic global vegetation models (DGVMs) typically represent key vegetation processes—such as photosynthesis and evapotranspiration—using a simplified classification of globally representative plant functional types (PFTs) that exhibit similar ecological and physiological traits (Gregor et al., 2024; Bergkvist et al., 2025). These are known as PFTs, and they are typically defined by traits including photosynthetic pathway (C3/C4), leaf morphology (needleleaf/broadleaf), and phenology (evergreen/deciduous) (Islam et al., 2024). Research has shown that explicitly incorporating forest restoration processes into DGVMs is critical not only for quantifying their feedback on the carbon cycle, surface energy balance, and the climate system, but also for providing a science-based foundation for policy assessment (Yue et al., 2024; Peng et al., 2024a). To accurately simulate carbon dynamics and vegetation succession, this requires the models to be driven by annually updated PFT distribution data (Pugh et al., 2024). However, a high-resolution, annual time-series dataset that accurately reflects the changes in PFT composition and spatial patterns during China's recent forest restoration is currently lacking (Yu et al., 2022; Xia et al., 2023). Most existing forest cover products either provide only single-year classifications or offer PFT information at coarse temporal resolutions, failing to meet the annual input requirements of DGVMs (Ran et al., 2012). Furthermore, they often fail to capture the forest recovery trends documented by NFI. While some recent studies have developed NFI-based reconstructed forest datasets, these products are typically either too coarse in spatial resolution (e.g., 0.5°), do not provide the distribution of individual PFTs, or are not temporally continuous, with maps produced only every several years (Yu et al., 2022; Xia et al., 2023). Therefore, there is an urgent need to generate NFI-consistent, high-resolution, and annually resolved long-term maps of both forest cover and PFT distribution. Such a dataset is fundamental for robustly assessing China's forest carbon sink and its driving factors using ecosystem models.

In this study, we developed a novel method that fuses the temporal constraints from statistical inventories with the spatial constraints from remote sensing data to identify the distribution of forest PFTs. We integrated provincial-level forest area statistics from the NFI for 1976–2021 with nearly all available LULC and auxiliary remote sensing products. This allowed us to first reconstruct annual changes in China's total forest cover at a 1 km spatial resolution from 1980 to 2023. Building on this foundation, we then derived the annual distribution of eight distinct PFTs for the period 1981–2013 through a series of systematic steps, including the classification of life forms and the derivation of phenological characteristics. The overall goal of this work is twofold: first, to provide a dataset that accurately captures the spatiotemporal distribution and trends of China's forests and PFTs since the onset of its national restoration programmers in the 1980s; and second, to demonstrate the effectiveness of this new dataset in a DGVM. To achieve this, we applied our product in the Lund–Potsdam–Jena General Ecosystem Simulator (LPJ-GUESS) model (Lindeskog et al., 2021) and benchmarked its performance against the global PFT dataset from the European Space Agency's Climate Change Initiative (ESA CCI) (Harper et al., 2023) in simulating key land

https://doi.org/10.5194/essd-2025-475
Preprint. Discussion started: 19 August 2025

surface variables (GPP, NEE, LAI, and ET). We present the following: (1) changes in China's forest cover and PFTs in China since the 1980s; (2) the historical dynamics of forest gain and loss, including their area, onset year, and duration; and (3) the performance of our reconstructed PFT distribution compared to existing global datasets when used in a DGVM. Ultimately, our dataset is expected to provide critical data support for the accurate simulation of China's forest carbon sink and the scientific assessment of its driving factors since the beginning of the nation's large-scale forest restoration.

2 Data

The forest cover and PFTs were derived from the integration of NFI data with multi-source remote sensing land cover time series data (Table 1, Table S1). The land cover data provides the spatial distribution of forest cover across different years. For specific years, the land cover classification also defined the extent of forest PFTs, based on distinctions in phenology and leaf morphology. The NFI data constrained the forest area and structural composition; this ensured that the resulting dataset aligned with reported national trends in forest area dynamics.

Auxiliary data products, such as the satellite-based normalized difference vegetation index (NDVI) data (see Sect. 2.3), were used to identify potential residual forest pixels in cases of discrepancy between the land cover data and NFI data. For example, where the forest cover extracted from the land cover data was less than the area specified by the NFI for a given region, NDVI was used as a sensitive indicator of vegetation vigor. Pixels considered more likely to represent forest cover were then selected to supplement the forest area and its spatial distribution.

Table 1. Summary of datasets used in this study.

Data Variable	Data Type	Resolution	Time	Data Source
NFI	Tabular Statistics	Provincial	1976–2021	National Forestry and Grassland Science Data Center (https://www.forestdata.cn/)
Multi-source LULC Products	Raster	Various, resampled to 1 km	1980–2023	See Supplementary Table1
Jeong's NDVI	Raster	0.05°	1982–2021	Jeong et al. (2024)
Climate Zones	Raster	~1 km (0.0083°)	1980–2016	(Beck et al., 2018)
Topographic	Raster	1 km	Static	Amatulli et al. (2018)
ERA5–Land	Raster	0.1°	1980–2023	Copernicus Climate Data Store (https://cds.climate.copernicus.eu/)

2.1 National Forest Inventories

To assess the quantity, structure, function, and productivity of its forest resources, the National Forestry and Grassland Administration of China conducted ten national forest resource inventories between 1973 and 2023. The inventories took place during the periods 1973–1976, 1977–1981, 1984–1988, 1989–1993, 1994–1998, 1999–2003, 2004–2008, 2009–2013, 2014–2018, and 2019–2021. The data are available from the National Forestry and Grassland Science Data Center (NFGSDC) at

https://doi.org/10.5194/essd-2025-475
Preprint. Discussion started: 19 August 2025

https://www.forestdata.cn/ (last access: 20 June 2025). The surveys were performed at the provincial level, employing a systematic sampling design with fixed plots located at the intersections of the national 1:50,000 or 1:100,000 topographic map grids. For each plot, recorded variables included forest cover, forest type area, and standing volume. This study utilized provincial-level forest area statistics from the first to the tenth NFI reports. These statistics comprise data for needleleaf forests, broadleaf forests, bamboo forests, and economically important timber forests.

2.2 Land use and land cover datasets

This study utilized nineteen datasets covering the period 1980–2023 as the foundational inputs for the forest cover reconstruction (Table S1). Forest cover information was extracted from these LULC products. Pre-processing of the data involved several steps: (i) reprojecting all datasets to the WGS_1984_Albers spatial reference system; (ii) resampling to a 1 km resolution using the nearest neighbor method; and (iii) aligning all data to a common grid framework to ensure a consistent cell size and spatial extent for China.

2.3 Satellite-based vegetation index dataset

This study utilized the global long-term NDVI dataset developed by Jeong et al. (2024), which was produced by fusing data from AVHRR and MODIS. The dataset is publicly available at: https://www.environment.snu.ac.kr/data/longterm-vi (last access: 13 April 2025). The product addresses temporal inconsistencies between sensors via cross-calibration of the AVHRR instruments, correction for orbital drift, and the fusion of AVHRR and MODIS data using machine learning techniques. It possesses a spatial resolution of 0.05° and a monthly temporal resolution, covering the period 1982–2021. In this study, the maximum growing-season NDVI value served as the primary indicator for classifying “potential forest pixels” of a given consistency level as forest (see Sect. 3.2). To extend the analysis period to 1980–2023 whilst maintaining continuity, the time series was gap-filled at its ends: records for 1980–1981 were substituted with data from 1982, and records for 2022–2023 were substituted with data from 2021.

2.4 Zonation products

To assign phenological types to the small number of remaining unclassified forest pixels (see Sect. 3.3.2), two supplementary regional partitioning products were utilized. The first was the Köppen–Geiger climate classification from Beck et al. (2018), which classifies Earth’s land surface into 30 distinct climate zones at a 0.0083° resolution (approx. 1 km) based on temperature and precipitation records from 1980–2016. The data are publicly available from Figshare at: https://figshare.com/articles/dataset/Present_and_future_K_ppen-Geiger_climate_classification_maps_at_1-km_resolution/6396959/2 (last access: 26 May 2025). The second product was a global topographic dataset from Amatulli et al. (2018), derived from the 250 m GMTED2010 and 90 m SRTM4.1dev digital elevation models. This dataset classifies the global land surface into ten topographic categories: flat, peak, ridge, shoulder, spur, slope, hollow, footslope, valley, and pit. The data are publicly available from Earthenv at: https://www.earthenv.org/topography (last access: 25 May 2025). Generally,

https://doi.org/10.5194/essd-2025-475
Preprint. Discussion started: 19 August 2025

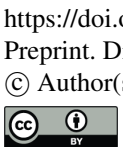

needleleaf forests are predominantly evergreen, with the notable exception of larch forests, which are deciduous and found mainly in boreal regions. In contrast, broadleaf forests are typically deciduous, although those in tropical regions are predominantly evergreen. To further classify evergreen and deciduous forest types as either boreal/temperate or tropical (see Sect. 3.3.3), this study also utilized 2 m temperature data from the ERA5–Land reanalysis dataset. This dataset provides monthly mean climate variables at a 0.1° spatial resolution, covering the temporal range 1980–2023. The data are publicly available from the Copernicus Climate Data Store at: https://cds.climate.copernicus.eu/datasets/reanalysis-era5-land-monthly-means?tab=overview (last access: 21 September 2024).

3 Method

The framework for mapping forest cover and PFTs is shown in Fig. 1. It includes the interpolation of NFI statistical data, reconstruction of annual forest cover, validation, and modelling assessment. We constructed annual forest cover maps of China for the period 1980–2023 by integrating multiple data sources and derived PFTs through a sequential, multi-step process: first, forest life forms were classified using a method analogous to the forest cover reconstruction, second, deriving phenological characteristics, and finally, subdividing these intermediate classifications into the final PFTs based on a set of climatic rules. Notably, the availability of NFI data for needleleaf and broadleaf forests is restricted to the period 1981–2013. Consequently, the corresponding annual PFT maps were reconstructed only for these years. Finally, the accuracy of the reconstructed dataset was assessed using validation samples from field surveys and independent reference data, and its consistency was analyzed against existing LULC datasets. In particular, the reconstructed PFT dataset was used to drive a DGVM to evaluate the performance of the updated PFTs in simulating a series of surface fluxes by comparing them against those from a simulation using the global PFT dataset from the ESA CCI (Harper et al., 2023).

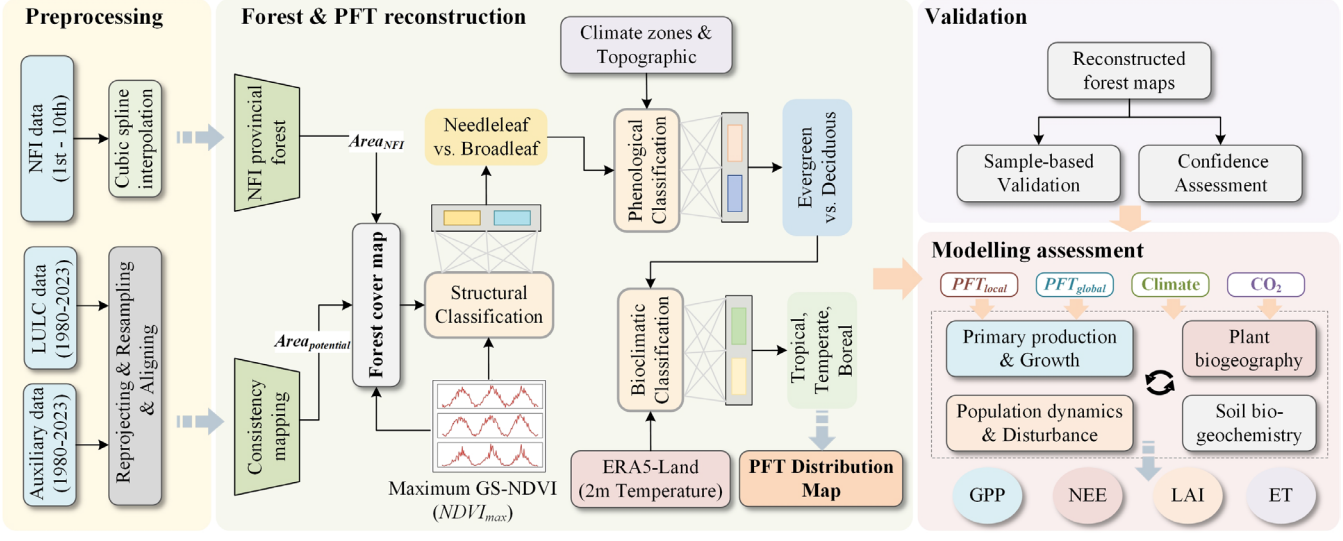

Figure 1. Flowchart for generating annual forest cover and PFT maps.

https://doi.org/10.5194/essd-2025-475
Preprint. Discussion started: 19 August 2025

3.1 Interpolation of NFI statistical data

For the construction of the 1980–2023 forest cover time series, the provincial-level forest area from each NFI period was assigned to the final year of that period (e.g., data from the 1973–1976 survey were assigned to the year 1976) (Yue et al., 2024). Given the non-uniform time intervals of the NFI data and the potential for non-linear trends in provincial forest area, cubic spline interpolation was employed. This piecewise method constructs a series of cubic polynomials between data points and ensures continuity in the first and second derivatives, making it well-suited to handling non-uniform intervals whilst providing a high-quality fit and smooth trend lines. Cubic spline interpolation was used to infill missing forest area data for the period 1976–2021, whilst the Holt-Winters exponential smoothing method was applied to forecast data for 2022 and 2023. Owing to provincial-level differences in policy and other influencing factors, the interpolation and forecasting were performed independently for each province (Fig. S1).

For Hong Kong, Macau, and Chongqing, comprehensive statistical data were only available from 2003 onwards, which necessitated data extrapolation for the period 1980–2002. Linear regression was used to estimate the historical forest area for these regions, adopting a methodology similar to that of Yu et al. (2022) and Yue et al. (2024) (Fig. S1). To mitigate the uncertainty inherent in this approach, the extrapolated values were not used directly to define the historical forest extent (e.g., Fig. S1, Chongqing). Instead, the forest area value from the consistency-level raster (see Sect. 3.2) that most closely matched the extrapolated estimate was identified, and its corresponding spatial extent was used as the forest mask for that year.

3.2 Forest cover reconstruction

Rather than adopting traditional biophysical definitions of "forest" (e.g., canopy cover ≥ 10%, tree height ≥ 5 m) or adhering to a single classification standard from the FAO or national bodies, this study developed a data-driven "forest consistency" method to reconstruct historical forest cover (Fig. 1). The method involved overlaying all available LULC datasets for each year (Fig. S2). For any given pixel, "consistency" (CON) was defined as the number of datasets that classified it as forest (Fig. S3a). A pixel was subsequently identified as a "potential forest pixel" if it was classified as forest in at least one dataset (i.e., $CON > 0$). The consistency value was then used to establish priority, whereby a higher CON value indicated a greater likelihood of the pixel representing true forest cover (Xia et al., 2023; Fang et al., 2020).

To determine the consistency threshold for the final forest classification, all potential forest pixels were ranked in descending order of their CON value. The NFI–derived area for a given province was used as the target value to establish this threshold. Specifically, two scenarios were considered. First, if the total area of all potential forest pixels were less than the NFI-reported area, all potential pixels were classified as forest, a scenario which could result in an underestimation for that province. Second, if the total area of potential pixels exceeded the NFI-reported area, a cumulative summation was performed. Pixels were incrementally summed, starting from the highest consistency value downwards, until the cumulative area bracketed the NFI target area (A_{NFI}). If the cumulative area of pixels with $CON \geq m$ was less than A_{NFI}, but the cumulative area of pixels with $CON \geq m - 1$ exceeded A_{NFI}, then m was defined as the consistency threshold. All pixels with a consistency

https://doi.org/10.5194/essd-2025-475
Preprint. Discussion started: 19 August 2025

value ≥ m were subsequently classified as forest. To precisely match the NFI target area, however, a portion of the remaining required area was fulfilled by selecting pixels from the $CON = m - 1$ level. Based on the assumption that, within a given consistency level, a higher NDVI value indicates a greater likelihood of forest cover, the maximum growing-season NDVI ($NDVI_{max}$) was calculated for all pixels at the $CON = m - 1$ level. These pixels were then ranked in descending order of their $NDVI_{max}$ value. The top n pixels were subsequently selected as "residual forest pixels", where n was determined by the remaining area required to precisely match the NFI target.

In summary, the final forest classification identified pixels exhibiting both high cross-dataset consistency and high growing-season NDVI values. The total area of this final classification was strictly constrained by provincial NFI statistics, thereby ensuring the reconstructed maps align with the authoritative inventory data. While this method generally ensures a close correspondence to the NFI-reported area, a minor systematic underestimation can occur. This is a consequence of pixel resolution limitations, particularly when the final area required to meet the NFI target is smaller than that of a single pixel.

3.3 PFT dataset development

3.3.1 Distinguishing between needleleaf and broadleaf forest types

Theoretically, the same reconstruction method used for total forest cover could be applied to directly classify four distinct PFTs: evergreen needleleaf, evergreen broadleaf, deciduous needleleaf, and deciduous broadleaf forests. However, data availability constraints preclude the direct application of this method, since few LULC products offer this level of thematic detail, particularly for periods before 1990. For instance, for the year 1985, only a single available dataset differentiated between needleleaf and broadleaf forests, while for 1980, no dataset provided phenological classifications (i.e., evergreen vs. deciduous, Table S1). Consequently, a foundational assumption of this study is that the relative spatial distribution of these four PFTs remained static over the analysis period.

The NFI provides provincial-level forest area statistics for needleleaf and broadleaf forests for the period 1981–2013, but it lacks phenological classifications (i.e., evergreen vs. deciduous). Therefore, the initial classification step in this study was to distinguish between needleleaf and broadleaf forests within the previously reconstructed total forest extent.

To achieve this, seven LULC products containing forest type information were selected (Table S1). All available temporal layers from these seven products, amounting to 73 distinct data layers in total, were subsequently overlaid. Adhering to the previously stated assumption of a static PFT distribution, these 73 layers were used to generate two static consistency maps: one for needleleaf and one for broadleaf forests (Fig. S4). To ensure close spatial correspondence between this PFT classification and the main forest cover dataset, the static consistency maps were masked using the annual 1 km forest extent maps. This process generated annual consistency maps for each forest type, constrained within the total forest area for each respective year.

A critical preliminary step was required to adapt the main reconstruction method for distinguishing between needleleaf and broadleaf forests. The primary goal of this step was not to produce a final classification, but to resolve conflicts among the

https://doi.org/10.5194/essd-2025-475
Preprint. Discussion started: 19 August 2025

Open Access Earth System Science Data Discussions

source LULC datasets. This ensured that each pixel could be assigned a single, spatially exclusive 'type-specific consistency' value, which is a prerequisite for the reconstruction logic that follows.

To achieve this, two consistency values were calculated for each pixel: needleleaf consistency (CON_{need}), representing the number of LULC datasets classifying the pixel as needleleaf forest; and broadleaf consistency (CON_{broa}), representing the number of datasets classifying it as broadleaf forest. A rule-based approach was then applied to handle the three possible scenarios and assign a preliminary, exclusive status to each pixel:

1. Both consistency values are non-zero ($CON_{need} > 0$ and $CON_{broa} > 0$): The pixel's consistency type was determined by comparing the two values. If $CON_{need} > CON_{broa}$, the pixel was designated as a needleleaf consistency pixel. If $CON_{need} < CON_{broa}$, it was designated as a broadleaf consistency pixel. If $CON_{need} = CON_{broa}$, the pixel was flagged as 'ambiguous', and its classification was deferred to a later stage.

2. Only one consistency value is non-zero (e.g., $CON_{need} > 0$ and $CON_{broa} = 0$): The pixel was designated as a consistency pixel of the corresponding forest type for which the value existed.

3. Both consistency values are zero ($CON_{need} = 0$ and $CON_{broa} = 0$): The pixel was provisionally flagged as "unclassified forest type" in this step, with its final status to be determined later.

The second major step was to generate annual distribution masks for needleleaf and broadleaf forests for each province for the period 1981–2013. This was achieved by integrating provincial NFI area statistics with the type-specific consistency information. In a process analogous to the total forest cover reconstruction, the NFI area statistics for needleleaf and broadleaf forests were used as annual targets. The specific allocation logic, which uses NDVI data as a secondary criterion, depended on the relationship between the consistency-derived area and the NFI target area. This resulted in three distinct cases:

1. Both forest types have "valid" consistency data (i.e., the total potential area from the consistency map exceeds the NFI target area). In this scenario, the allocation method described previously was applied independently to each type. The consistency threshold (m) was determined, and the remaining area required to meet the NFI target was fulfilled by selecting pixels from the $CON = m - 1$ level, ranked in descending order of their $NDVI_{max}$ value.

2. Only one forest type has "valid" consistency data. The "valid" type was processed first, following the same procedure as in Case 1. For the "invalid" type (where the potential area was less than the NFI target), a hierarchical sourcing strategy was used to fulfill its NFI area target. Pixels were drawn sequentially from the following pools, using the NDVI-ranking method for selection at each stage:

First, from pixels flagged as "ambiguous" ($CON_{need} = CON_{broa}$).

Second, from a pixel pool generated using the "valid" type's unallocated pixels. This involved using the "remainder" pixels from the "valid" type's consistency map (i.e., those not selected to meet its own NFI target) to mask the original consistency map of the "invalid" type. From this newly masked map, pixels were then selected in descending order of their consistency value until the NFI area target for the "invalid" type was fulfilled.

Third, from pixels flagged as an "unclassified forest type".

https://doi.org/10.5194/essd-2025-475
Preprint. Discussion started: 19 August 2025

3. Neither forest type has "valid" consistency data. In this case, both NFI area targets were fulfilled by drawing pixels exclusively from the "ambiguous" and "unclassified forest type" pools. The allocation was prioritized for the provincially "dominant" type (i.e., the type with the larger NFI area). Once its target was met, the remaining pixels from these pools were allocated to the other forest type. The NDVI-ranking method was used for all selections.

Finally, this process resulted in the output of annual needleleaf and broadleaf forest distribution masks for the specified period.

3.3.2 Distinguishing between evergreen and deciduous phenological types

In a process analogous to the classification of needleleaf and broadleaf types, a further classification was performed to distinguish between evergreen and deciduous phenologies. This step utilized a new set of consistency rasters that classified pixels based on both life form and phenological type (Fig. S5). However, as the NFI dataset lacks area statistics for these phenological types, no area-based constraints could be applied. Instead, the classification was performed directly within the masks delineated in the previous step. For example, evergreen and deciduous needleleaf forests were identified from within the total needleleaf mask based solely on their respective consistency values. An identical operation was performed for broadleaf forests. Any pixel within a given life-form mask (i.e., needleleaf or broadleaf) that could not be assigned a phenological type was designated as a "residual" pixel (e.g., "residual needleleaf") and reserved for subsequent processing.

The previously generated consistency masks were then used to refine the phenological classification within the needleleaf and broadleaf categories. This was achieved through a pixel-level comparison of type-specific consistency values. The process is illustrated below using the example of distinguishing between deciduous broadleaf forest (DBF) and evergreen broadleaf forest (EBF).

1. Pixel has competing classifications: Where a pixel possessed a non-zero consistency value for both deciduous (CON_{DBF}) and evergreen (CON_{EBF}) broadleaf types, a direct comparison was made：

If $CON_{DBF} > CON_{EBF}$, the pixel was classified as DBF. If $CON_{DBF} < CON_{EBF}$ the pixel was classified as EBF. If $CON_{DBF} = CON_{EBF}$, the pixel was not assigned a phenological type. Instead, it was designated as "residual broadleaf" and reserved for subsequent processing.

2. Pixel has a single classification: Where a pixel possessed a non-zero consistency value for only one phenological type (e.g., $CON_{DBF} > 0$ and $CON_{EBF} = 0$), it was classified accordingly as either DBF or EBF.

The classification of evergreen and deciduous needleleaf forests (ENF and DNF) followed an identical procedure to that of broadleaf forests. This initial stage resulted in the annual classification of four primary PFTs (DNF, ENF, DBF, EBF), alongside a category of "residual" pixels requiring further processing. This category comprised pixels confirmed as either needleleaf or broadleaf, but for which a phenological type could not yet be assigned. To resolve these pixels, two subsequent methods were employed: a neighborhood analysis and an environmental inference method.

https://doi.org/10.5194/essd-2025-475
Preprint. Discussion started: 19 August 2025

Neighborhood Analysis: For each "residual" pixel, a 10×10 pixel neighborhood window was established around it. Within this window, the total number of pixels belonging to each of the four classified PFTs (DNF, ENF, DBF, and EBF) was counted. The classification logic was then applied as follows:

For a "residual needleleaf pixel", the counts of DNF and ENF neighbors were compared. If the DNF count was greater, the pixel was classified as DNF. Conversely, if the ENF count was greater, the pixel was classified as ENF. If the DNF and ENF counts were equal, or if no classified needleleaf neighbors were present in the window, the pixel was flagged as "pending". An identical logic was applied to "residual broadleaf" pixels, based on the counts of their DBF and EBF neighbors.

Environmental Inference Method: For the small number of remaining "pending" pixels (typically those with no classified neighbors), an environmental inference method was used to assign a final phenology based on climatic and topographic data (see Sect. 2.4). The procedure involved the following steps: First, the climate zone and topography data were overlaid to create a map of unique "environmental strata" (i.e., unique combinations of climate and topography). Second, for each province and year, the relative proportion of the four PFTs was calculated within each unique environmental stratum. Third, a "pending" broadleaf pixel was assigned the phenological type (EBF or DBF) that was most prevalent within its specific environmental stratum, according to the calculated proportions. The same logic was applied to "pending" needleleaf pixels.

Finally, the classifications from all steps were merged to produce the annual distribution maps for the four PFTs (DNF, ENF, DBF, and EBF) for each province.

3.3.3 Final PFT classification

Adopting the methodology of Bonan et al. (2002) and utilising the historical climate data (see Sect. 2.4), the four preliminary forest types were further subdivided into eight final PFTs. The specific climatic variables used for this classification are detailed in Table 2 and include:

T_c is the mean temperature of the coldest month.

GDD (Growing Degree Days) are the annual cumulative temperature exceeding a 5℃ baseline.

The daily growing degree days (GDD_d) are calculated as follows:

$$GDD = \sum_{d=1}^{365} \max\left(T_d - T_b, 0\right) \quad (1)$$

Where:

T_d is the mean daily temperature, and T_b is the base temperature for growth, set at 5℃

Since daily mean temperature data are not available in the ERA5–Land product, an alternative method was employed to estimate GDD. This involved substituting the monthly mean temperature for T_d in Eq. (1) and then multiplying the result by the number of days in that month to yield a monthly GDD value. The annual GDD was subsequently calculated as the sum of these monthly values.

Through the sequence of methods detailed above, a comprehensive historical dataset of forest cover for China, classified by PFT, was produced.

https://doi.org/10.5194/essd-2025-475
Preprint. Discussion started: 19 August 2025

Table 2. Classification scheme for deriving PFTs from forest life forms and climatic rules.

Plant Functional Type	Forest type	Climate Rules
Needleleaf evergreen tree, temperate	needleleaf evergreen tree	T_c > -19°C and GDD > 1200
Needleleaf evergreen tree, boreal	needleleaf evergreen tree	T_c ≤ -19°C or GDD ≤ 1200
Needleleaf deciduous tree	needleleaf deciduous tree	none
Broadleaf evergreen tree, tropical	broadleaf evergreen tree	T_c > 15.5°C
Broadleaf evergreen tree, temperate	broadleaf evergreen tree	T_c ≤ 15.5°C
Broadleaf deciduous tree, tropical	broadleaf deciduous tree	T_c > 15.5°C
Broadleaf deciduous tree, temperate	broadleaf deciduous tree	-15°C < T_c ≤ 15.5°C and GDD > 1200
Broadleaf deciduous tree, boreal	broadleaf deciduous tree	T_c ≤ -15°C or GDD ≤ 1200

3.4 Validation

The accuracy of the reconstructed forest cover maps was validated using independent field survey data. The validation was conducted in two stages: first for needleleaf and broadleaf forest types, and subsequently for the total forest area. Two primary sources of data were used for this validation. The first was the global all-season sample set from Li et al. (2017), the first of its kind, developed from Landsat-8 data. Generated through visual interpretation in Global Mapper software, this global dataset contains approximately 340,000 training samples (~90,000 locations) and 140,000 validation samples (~36,000 locations). For the present study, a subset was selected, comprising forest samples from 2014 and 2015 within the study area. Additionally, samples from land types commonly confused with forest (e.g., cropland and grassland) were aggregated into a single "non-forest" category. This process yielded 1,412 forest and 2,591 non-forest samples from this source. The second source was a nationwide field survey conducted between 2011 and 2013, which recorded plot-level details including vegetation type. From this field campaign, 2,860 independent validation samples for needleleaf and broadleaf forest types were obtained, comprising 1,433 broadleaf and 1,427 needleleaf forest samples. Combining these sources resulted in a final validation dataset of 6,863 independent samples (Fig. S6). This dataset was used to generate confusion matrices and calculate overall accuracy (OA), user's accuracy (UA), producer's accuracy (PA), and the F1-score for the reconstructed maps.

In addition to this sample-based validation, an indirect accuracy assessment was performed by analyzing the consistency among the input LULC datasets. This approach is pertinent as the final product is an integration of these sources. Here, consistency is defined at the pixel level as the number of LULC datasets that concur on the classification of a specific forest type. The underlying assumption of this analysis is that a higher consistency value for a given pixel indicates greater confidence in its classification and a higher likelihood of it being correct (Xia et al., 2023).

3.5 Forest change analysis

Forest change is defined as the transition of land cover between forest and non-forest states over a given period. It is typically classified into change events (i.e., forest gain or loss) and stable states (i.e., persistent forest or persistent non-forest) (Winkler et al., 2021). Forest gain represents a transition from a non-forest to a forest state, while forest loss is the reverse process

https://doi.org/10.5194/essd-2025-475
Preprint. Discussion started: 19 August 2025

(Hansen et al., 2013). To identify the onset year and duration of forest change events across China for the period 1980–2023, a pixel-level time-series analysis was developed based on the annual forest mask sequence.

This methodology is illustrated here using the detection of forest gain. First, the annual forest masks were standardized into binary values (0 = non-forest; 1 = forest) to create a spatiotemporal data cube. For this analysis, a "stable" forest state was defined as a pixel remaining as forest for at least three consecutive years (Yang and Song, 2023). The onset year of a forest gain event was then identified for each pixel as the first year it transitioned from a non-forest state to a stable forest state.

Following the identification of a gain event, the duration of forest persistence was calculated. This duration is the number of years from the onset of the gain until either: (a) the pixel underwent a stable loss event, defined as transitioning to non-forest and remaining so for at least three consecutive years, or (b) the end of the study period (2023) if no such loss event occurred. The detection of forest loss events and their duration followed the inverse logic.

This analysis produced four maps: two indicating the onset year for forest gain and loss events, and two representing the duration of these respective periods.

3.6 Modelling assessment

The impact of the new PFT distribution on surface fluxes was assessed using LPJ–GUESS (Lindeskog et al., 2021), a process-based DGVM. The primary objective of the simulation was to evaluate how the updated PFT map influences key carbon and water fluxes at the land surface.

To isolate the effect of the PFT distribution, two distinct model experiments were conducted. Both experiments were driven by identical climate forcing data from the ERA5–Land reanalysis product (including temperature, precipitation, and downward shortwave radiation) for the period 1981–2013. The crucial difference between the experiments was the PFT input map:

EXP1 utilised the new PFT map developed in this study.

EXP2 utilised the global PFT dataset from ESA CCI as a baseline for comparison.

In both experiments, the PFT distribution from the year 2010 was applied cyclically for each year of the simulation to maintain a static land cover driver. The LPJ–GUESS model was run at a 0.1° × 0.1° spatial resolution. The simulation period was 1981–2013; model outputs before 1981 were considered part of the "spin-up" phase and were discarded from the analysis.

The outputs from the two experiments were compared for the China region across a range of land surface variables, including gross primary productivity (GPP), net ecosystem exchange (NEE), leaf area index (LAI), and actual evapotranspiration (ET). As the PFT map was the sole variable altered between the two experiments, any observed differences in the output fluxes could be directly attributed to its influence.

https://doi.org/10.5194/essd-2025-475
Preprint. Discussion started: 19 August 2025

Open Access Earth System Science Data Discussions

4 Results

4.1 Accuracy assessment of the reconstructed forest cover dataset

Validation based on field survey data from five time points shows that for the total forest classification, the overall accuracy in 2014 and 2015 was 94.79 ± 0.49% and 95.74 ± 0.53%, respectively, while the user's accuracy for forest types in these two years was 93.65 ± 0.81% and 94.11 ± 1.06%, respectively (Table 3). For the period 2011–2013, the overall accuracy for needleleaf forests ranged between 84.35 ± 1.6% and 90.18 ± 2.3%, while for broadleaf forests, the range was 85.41 ± 1.5% to 92.02 ± 2.16%. The F1-score for broadleaf forests was slightly higher than for needleleaf forests (Table 4). We also found that the reconstructed broadleaf forests exhibited higher consistency than the needleleaf forests (Figure S3b, S3c). Notably, according to our methodology, a pixel-weighted average over the 1980–2023 period indicates that approximately 6.9% of pixels in the reconstructed needleleaf forests and 2.7% in the reconstructed broadleaf forests did not fall within their corresponding consistency type.

Table 3. Confusion matrix for the reconstructed total forest cover classification for 2014 and 2015.

Year	Reference	Classification		User's Accuracy (%)	Producer's Accuracy (%)	F1-Score (%)	Overall Accuracy (%)
		Forest	Non-forest				
2014	Forest	841	72	93.65±0.81	92.11±0.89	92.88	94.79±0.49
2014	Non-forest	57	1508	95.44±0.52	96.36±0.47	95.9	
2015	Forest	463	36	94.11±1.06	92.79±1.16	93.44	95.74±0.53
2015	Non-forest	29	997	96.52±0.57	97.17±0.52	96.84	

Table 4. Confusion matrices and accuracy metrics for the needleleaf and broadleaf forest classifications for the period 2011–2013.

Year	Reference	Classification		User's Accuracy (%)	Producer's Accuracy (%)	F1-Score (%)	Overall Accuracy (%)
		broadleaf	needleleaf				
2011	broadleaf	420	90	87.32±1.52	82.35±1.69	84.76	85.41±1.5
2011	needleleaf	118	407	90.24±1.4	77.52±1.82	83.4	84.35±1.6
2012	broadleaf	644	98	92.4±1	86.79±1.24	89.51	89.93±1.11
2012	needleleaf	115	642	93.18±0.96	84.81±1.31	88.8	89.19±1.18
2013	broadleaf	170	11	91.89±2.01	93.92±1.78	92.9	92.02±2.16
2013	needleleaf	27	118	95.93±1.79	81.38±3.24	88.06	90.18±2.3

The internal consistency of the reconstructed total forest cover was assessed at ten specific time points: 1980, 1985, 1990, 1995, 2000, 2005, 2010, 2015, 2020, and 2023 (Fig. 2). The number of inputs LULC datasets available for the reconstruction varied at each time point, with 4, 6, 5, 6, 9, 10, 9, 9, 10, and 4 products used for each respective year. The analysis showed that for each of the ten time points, 87.3%, 70.8%, 82.9%, 69.8%, 40.1%, 23.7%, 24.0%, 25.6%, 24.6%, and 35.2% of the reconstructed forest pixels, respectively, achieved the maximum possible consistency score. Conversely, pixels with the lowest

https://doi.org/10.5194/essd-2025-475
Preprint. Discussion started: 19 August 2025

possible consistency ($CON = 1$) consistently accounted for a small fraction of the total reconstructed forest area, ranging from 0.01% to 6.9% across different years (Fig. 2). Spatially, areas with lower forest consistency were predominantly located in the arid and semi-arid regions of northwestern China (e.g., Xinjiang, Qinghai, Ningxia) and the highly fragmented landscapes of the eastern coastal plains (e.g., Tianjin, Shandong, Jiangsu, Shanghai). In contrast, high-consistency forest areas were mainly concentrated in regions with extensive and stable forest cover, primarily in southern and central China, including provinces such as Hubei, Zhejiang, Guangxi, Guizhou, Yunnan, and Jiangxi (Fig. S6 and S7).

https://doi.org/10.5194/essd-2025-475
Preprint. Discussion started: 19 August 2025

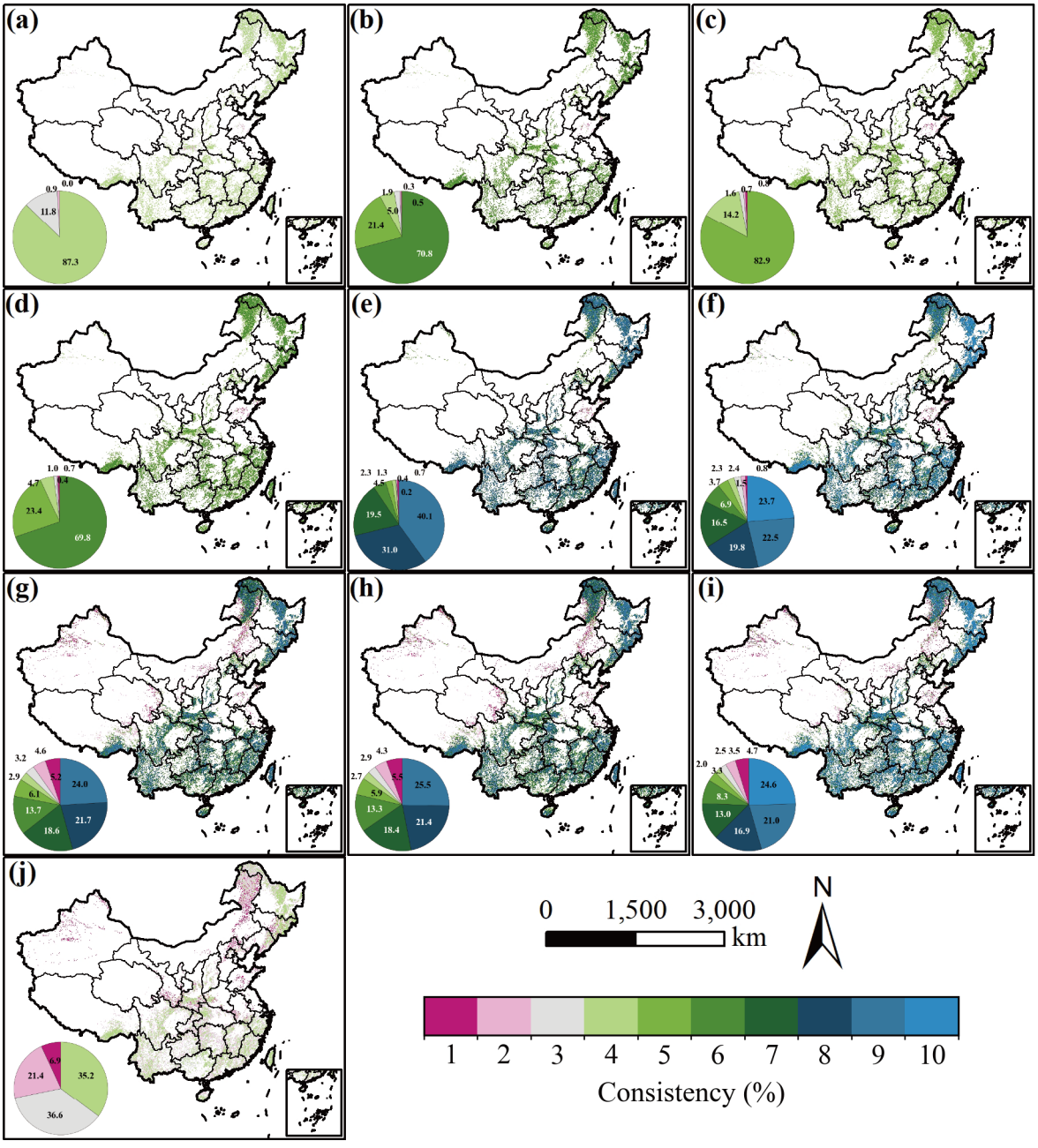

Figure 2. The spatial distribution of reconstructed forest cover is presented at five-year intervals from 1980–2023 **(a)** 1980, **(b)** 1985, **(c)** 1990, **(d)** 1995, **(e)** 2000, **(f)** 2005, **(g)** 2010, **(h)** 2015, **(i)** 2020, **(j)** 2023, along with corresponding cross-product consistency scores. The reconstruction for each time point was compared against an ensemble of data products sourced externally (n = 4, 6, 5, 6, 9, 10, 9, 9, 10, and 4, respectively). The inset pie chart (lower left) quantifies the areal proportion of the reconstructed forest dataset at various consistency levels, which serves as a proxy for the confidence in the resulting maps.

https://doi.org/10.5194/essd-2025-475
Preprint. Discussion started: 19 August 2025

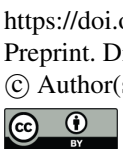

Open Access Earth System Science Data Discussions

A comparison and analysis of the NFI data with the forest area estimates reconstructed in this study at the provincial scale (Fig. 3) shows a good match for multiple years (1981–2021), with an R^2 close to 1 and a p-value < 10^{-27}. This indicates that the reconstructed data from this study is highly consistent with the NFI statistics in terms of overall trends. However, at the provincial level, slight discrepancies were still observed for some provinces (e.g., Inner Mongolia, Heilongjiang, Yunnan, and Xinjiang), where the reconstructed estimates in certain years were either slightly higher or lower than the NFI data. These discrepancies show a more pronounced trend after 2013.

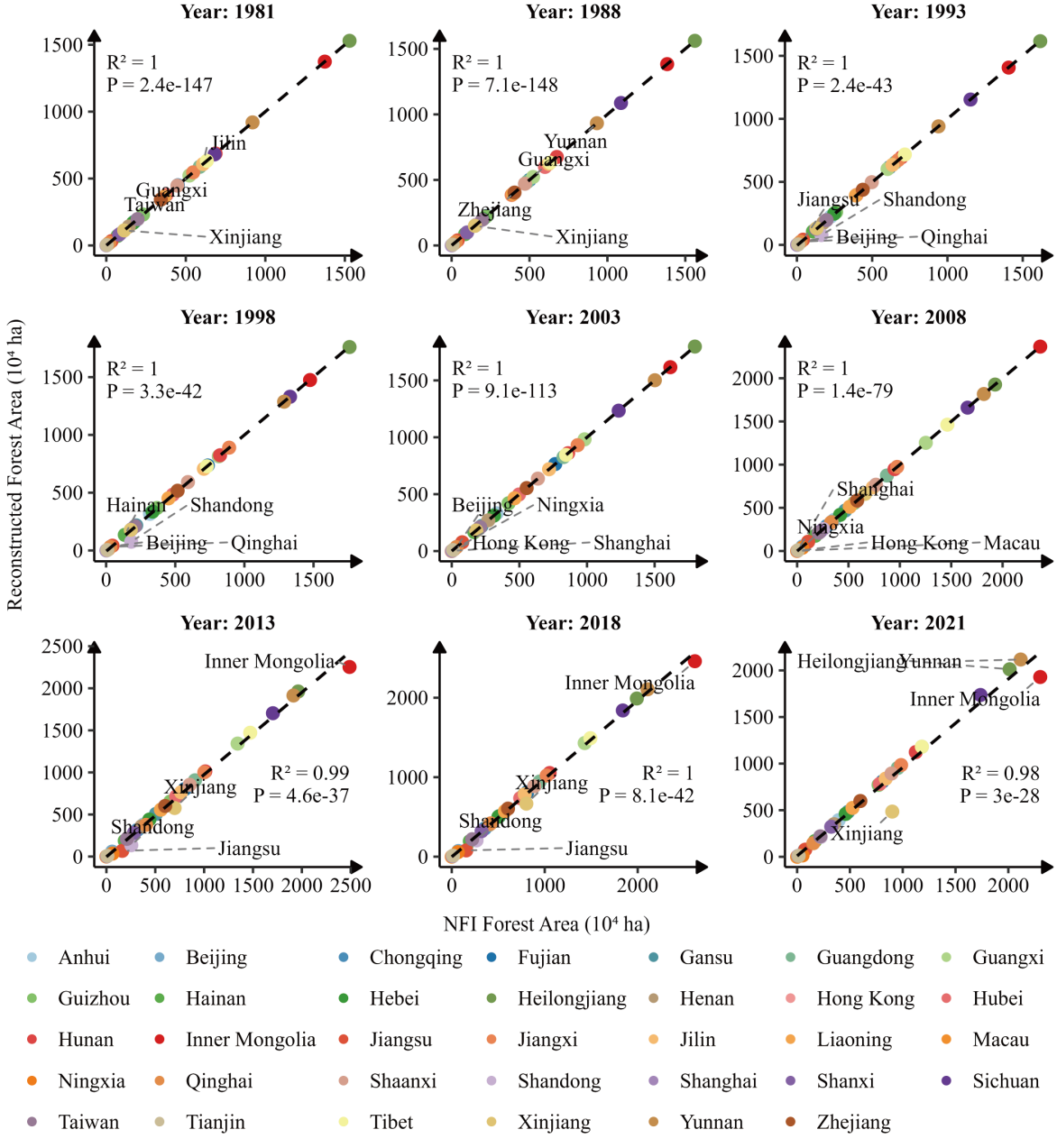

https://doi.org/10.5194/essd-2025-475
Preprint. Discussion started: 19 August 2025

Figure 3. Scatter plot comparing provincial-level forest area as reported by NFI with estimates from the reconstructed maps of this study.

4.2 Reconstructed Forest cover dataset description

This dataset provides annual forest cover distribution from 1980 to 2023 (Fig. 2) and the distribution of eight PFTs from 1981 to 2013 at a 1 km spatial resolution (Fig. 4). The data are supplied in the WGS 1984 Albers equal-area conic projection. The eight PFTs, are: (1) boreal evergreen needleleaf forest, (2) temperate evergreen needleleaf forest, (3) temperate evergreen broadleaf forest, (4) boreal deciduous broadleaf forest, (5) temperate deciduous broadleaf forest, (6) tropical deciduous broadleaf forest, (7) tropical evergreen broadleaf forest, and (8) deciduous needleleaf forest. The complete dataset is openly accessible at the Zenodo repository under the DOI 10.5281/zenodo.16208012 (Liu et al., 2025, last access: 20 July 2025).

For the reference year 2013, the dataset indicates that China's forests are composed of evergreen needleleaf forest (26.1%), deciduous broadleaf forest (23.4%), evergreen broadleaf forest (18.1%), and deciduous needleleaf forest (6.2%). Although temperate evergreen needleleaf and boreal deciduous broadleaf forests were the two largest components by area prior to 2000, their proportional contributions to the total forest area subsequently declined from 27.1% to 21.1% and from 19.2% to 14.2%, respectively. Conversely, the proportional representation of temperate evergreen broadleaf and temperate deciduous broadleaf forests expanded, increasing from 15.3% to 17.9% and from 6.4% to 8.9%, respectively (Fig. 4).

Spatially, the primary forest regions are concentrated in Northeast, Southeast, and Southwest China, whereas forest cover is relatively sparse in Northwest, Central, and East China. Furthermore, evergreen needleleaf and evergreen broadleaf forests are predominantly distributed across Southern China. Deciduous needleleaf forests are concentrated in the Greater Khingan Range in the northernmost part of Northeast China, while deciduous broadleaf forests are mainly located in Northeast China and the Qinling Mountains of Central China.

https://doi.org/10.5194/essd-2025-475
Preprint. Discussion started: 19 August 2025

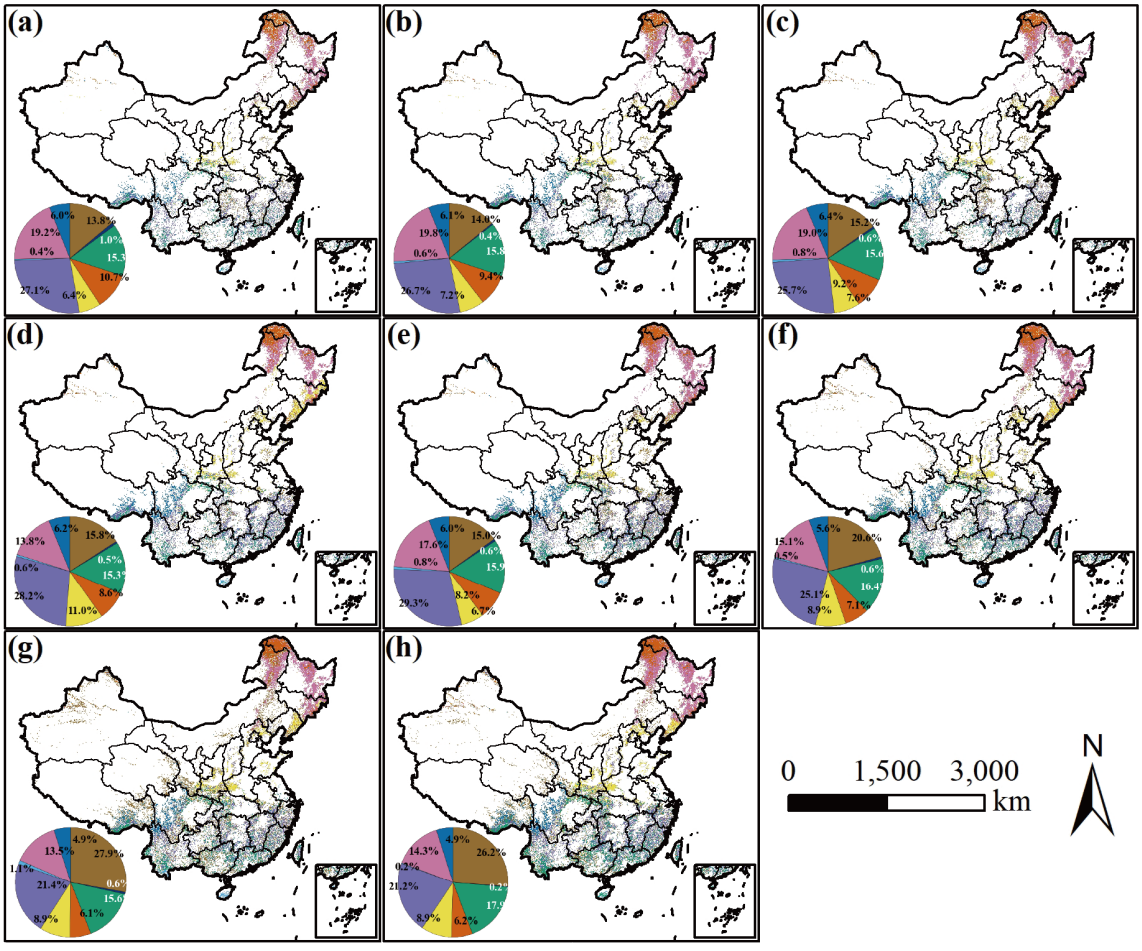

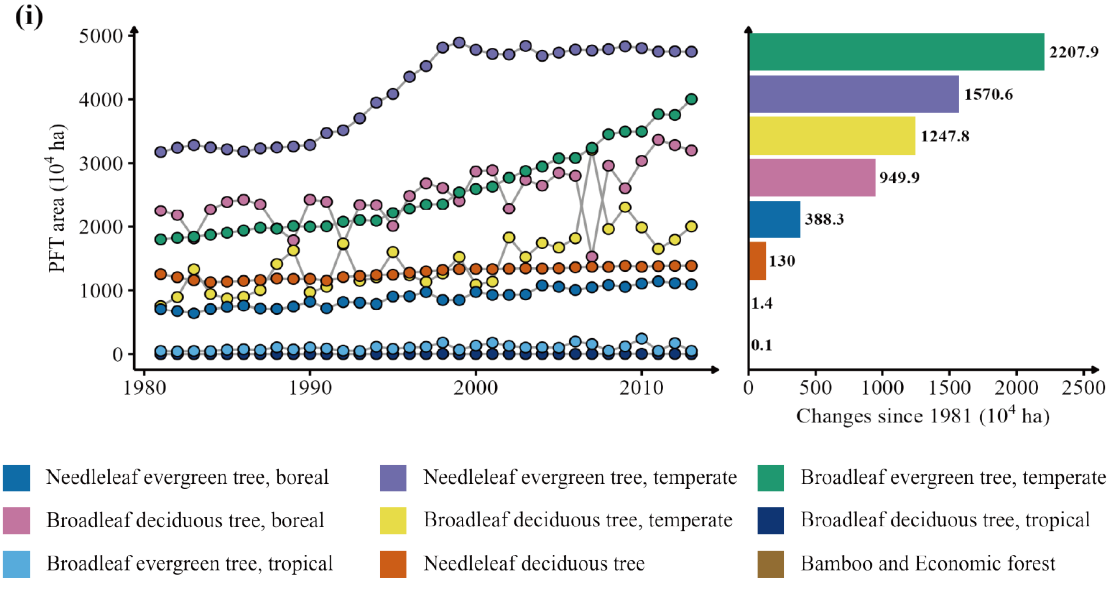

https://doi.org/10.5194/essd-2025-475
Preprint. Discussion started: 19 August 2025

Figure 4. Spatial distribution patterns and area proportions of China's forest PFTs for selected years between 1981 and 2013, **(a)-(h)** correspond to the years 1981, 1985, 1990, 1995, 2000, 2005, 2010, and 2013, respectively, **(i)** Temporal dynamics and total variation in PFTs from 1981 to 2013.

Regarding its temporal evolution, our reconstructed forest dataset faithfully reproduces the long-term dynamics of forest cover in China (Fig. 5). According to statistics from the NFI, China's forest cover has a mean annual growth rate of 1.75%. The reconstructed forest cover dataset reveals a substantial increase in China's total forest area from 117.14 million hectares (Mha) in 1980 to 213.15 Mha in 2023, with a peak of 236.50 Mha observed in 2020 (Fig. 5a). This represents an annualized growth rate of 1.82%, demonstrates strong agreement with this national benchmark. Furthermore, our dataset accurately captures the distinct historical trajectories of two principal forest categories–broadleaf and needleleaf forests–since the 1980s (Fig. 5b and 5c). This net increase was primarily propelled by the expansion of temperate and boreal forests. For example, the area of temperate evergreen broadleaf forest more than doubled between 1981 and 2013, increasing from 17.96 Mha to 40.04 Mha (Fig. 4i). During this period, significant areal gains were also recorded for temperate evergreen needleleaf, boreal deciduous broadleaf, and temperate deciduous broadleaf forests. In contrast, absolute changes in the extent of tropical PFTs and deciduous needleleaf forests were minimal over the same interval (Fig. 4i).

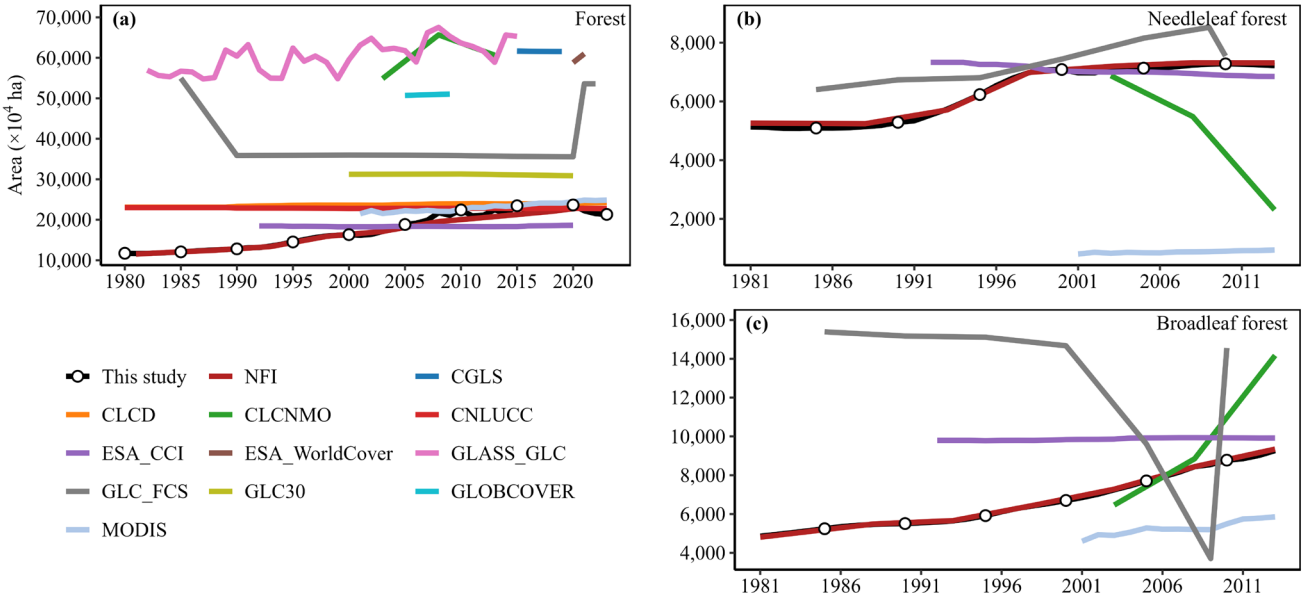

Figure 5. Temporal dynamics of national-scale total forest area, comparing the results of this study with data from NFI and other selected LULC products: **(a)** forest, **(b)** needleleaf forest, and **(c)** broadleaf forest.

4.3 Spatiotemporal patterns of forest cover change in China

Between 1980 and 2023, the total area experiencing forest change (gross change) amounted to 242.11 million hectares (Mha), equivalent to approximately 25% of China's terrestrial surface. This comprised 180.53 Mha of forest gain (19% of the national land area) and 153.48 Mha of forest loss (16% of the national land area). Forests that remained stable, persisting from 1980 to 2023, covered 572.77 Mha. This stable area represents 49% of the total forest extent in 1980, implying that the remaining 51%

https://doi.org/10.5194/essd-2025-475
Preprint. Discussion started: 19 August 2025

of the original 1980 forest cover underwent some form of change during the study period (Fig. 6q). We observed a prevalent pattern of forest change across several regions of China, characterized by a progression from more accessible areas (i.e., lower elevations near roads) to more remote locations (i.e., higher elevations far from roads). This dynamic often manifested as an core-to-edge expansion of existing forest patches (Fig. 6a-p). Temporally, both forest loss and gain were continuous dynamic processes throughout the entire period. A prominent peak in forest turnover occurred between 1991 and 1993, culminating in 1992 when the combined area of gain and loss surpassed 35 Mha. Post-2000, both gain and loss area exhibited a general downward trend, albeit with notable fluctuations. A moderate resurgence in turnover was observed between 2009 and 2011, after which forest loss and gain events tended to occur more concurrently (Fig. 6q).

Furthermore, our analysis reveals that events of forest loss are typically of short duration (Fig. S8). Over 35% of all observed losses persisted for only 3–6 years, with most loss events being transient and lasting fewer than 15 years. In contrast, forest gain is characterized by substantially longer persistence, with a modal duration of 31–34 years. This suggests the long-term stability of large tracts of newly established forests. The statistical distributions of persistence durations for forest gain and loss are markedly different. Loss events are predominantly concentrated in the shorter-duration intervals, whereas periods of gain are more concentrated in the medium- to long-duration brackets. This divergence indicates that newly established forests tend toward greater stability and longevity, while forest loss manifests as a more fragmented and ephemeral phenomenon.

https://doi.org/10.5194/essd-2025-475
Preprint. Discussion started: 19 August 2025

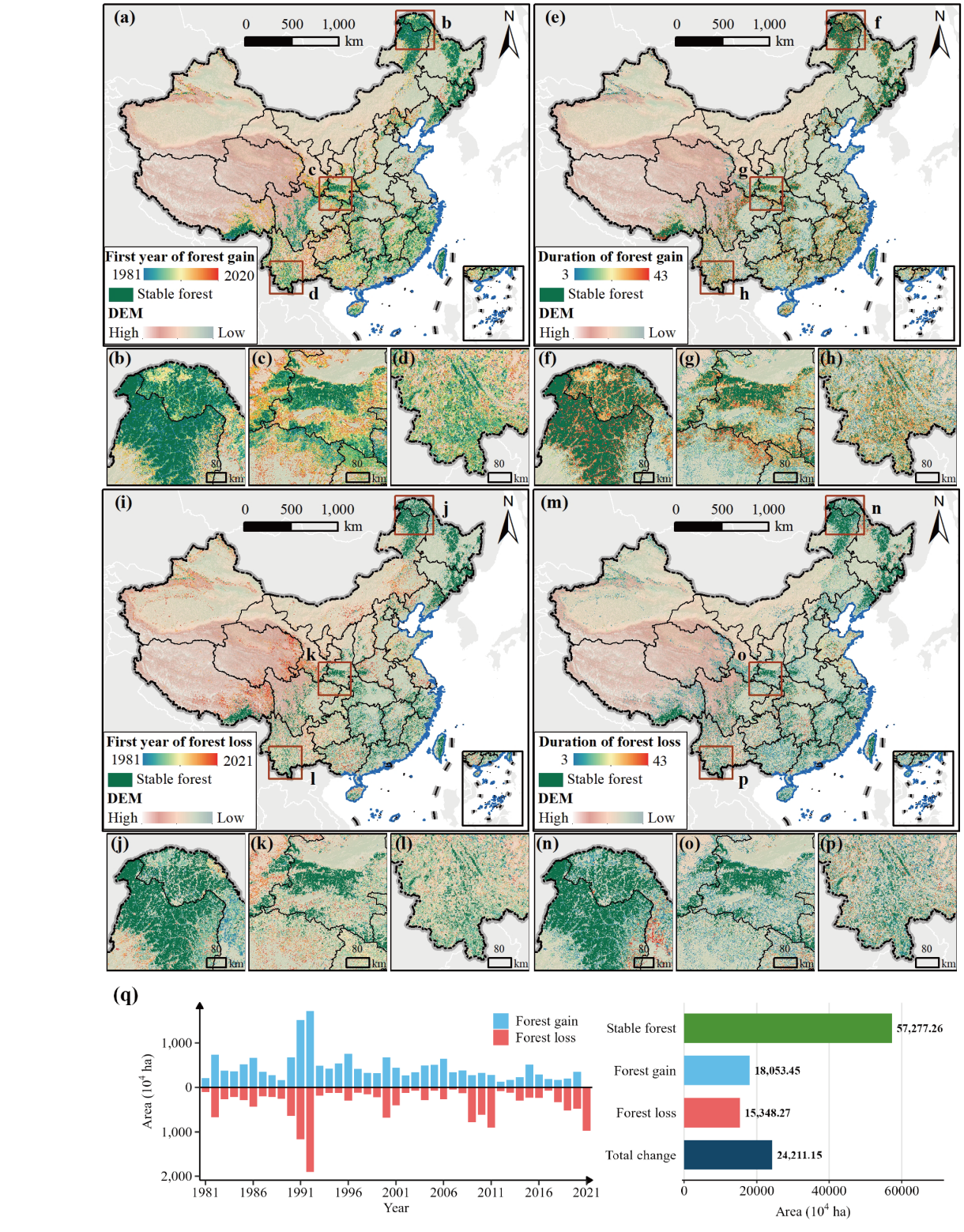

480

https://doi.org/10.5194/essd-2025-475
Preprint. Discussion started: 19 August 2025

Open Access Earth System Science Data Discussions

Figure 6. Spatio-temporal dynamics of forest gain and loss in China from 1980 to 2023. This figure presents: **(a-h)** the spatial patterns of forest gain, showing onset year and duration; **(i-p)** the spatial patterns of forest loss; and **(q)** the national-scale temporal dynamics, including the annual areas of forest gain and loss and a summary of total stable, gained, and lost forest areas.

4.4 Modelling results

We assessed the impact of different PFT forcing datasets on ecosystem simulations by comparing outputs from the LPJ–GUESS model driven by our reconstructed PFT product (hereafter PFT_{local}) versus the global PFT map from the European Space Agency (ESA) (hereafter PFT_{global}). The analysis, exemplified using data for the year 2010, quantifies the resulting differences in key ecosystem variables: GPP, NEE, LAI, and ET (Fig. 7). While annual-scale results are also presented (Fig. S9), we focus here on the mean differences (PFT_{local} minus PFT_{global}) during the summer period (June–August) to accentuate the primary impacts. The results indicate that the most marked divergences in simulated carbon and water fluxes are spatially coincident with regions where the two products show substantial differences in the fractional coverage of tree PFTs. Regions with a higher tree cover fraction in the PFT_{local} dataset relative to PFT_{global}, particularly in northeastern China (Fig. 7e, red), exhibit correspondingly elevated GPP, LAI, and ET, alongside a diminished NEE. Consequently, the resulting differentials are positive for the former variables and negative for NEE. Conversely, where the PFT_{global} dataset specifies greater tree coverage, such as in southwestern China (Fig. 7e, blue), these relationships are inverted.

https://doi.org/10.5194/essd-2025-475
Preprint. Discussion started: 19 August 2025

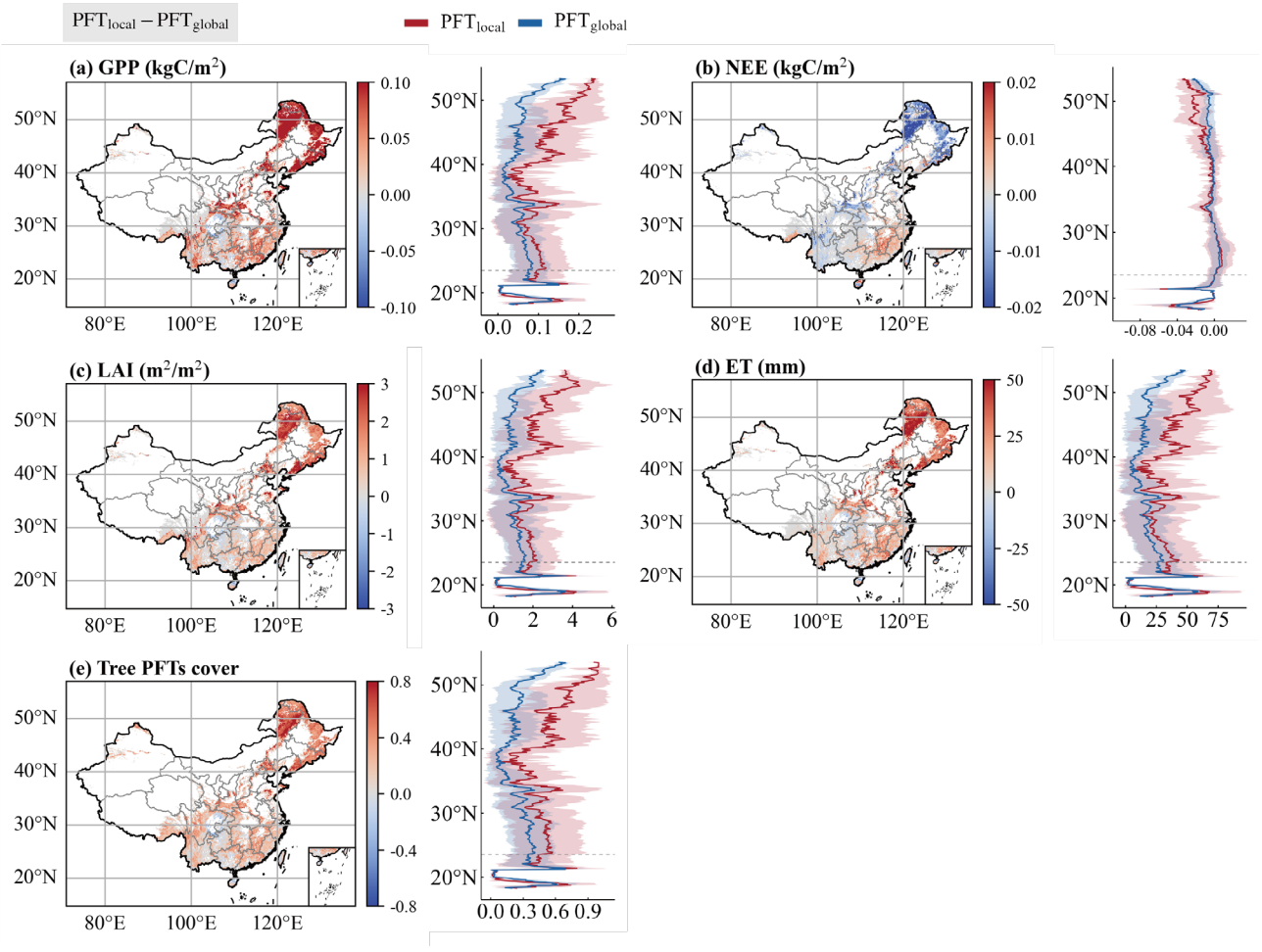

Figure 7. Comparison of LPJ–GUESS model simulations **(a–d)** and their underlying PFT forcing data **(e)** for summer 2010. The first four panels **(a–d)** show differences in simulated GPP, NEE, LAI, and ET. Panel **(e)** shows differences in tree PFTs cover derived directly from the input PFT maps. For all panels, the maps display the spatial difference ($\boldsymbol{PFT_{local} - PFT_{global}}$), while the plots show the zonal mean and standard deviation for the $\boldsymbol{PFT_{local}}$ (red) and $\boldsymbol{PFT_{global}}$ (blue) datasets individually. Note that data in panels **(a-d)** are model outputs, whereas data in panel **(e)** are from the input maps.

To assess the realism of the simulations, we benchmarked the model outputs against a suite of remote sensing-based products (FLUXCOM GPP, FLUXCOM NEE, GIMMS LAI4g, and GLEAM ET), with all datasets aggregated to a common 0.1° resolution (Fig. 8 for summer, June–August; Fig. S10 for the annual scale). In Fig. 8a and 8b, we first present a direct comparison between the surface fluxes simulated using our reconstructed PFT map (PFT_{local}) and the observational benchmarks. This baseline comparison highlights inherent discrepancies attributable to both structural biases in the LPJ–GUESS model and uncertainties within the remote sensing products themselves. Fig. 8c then isolates the impact of the PFT forcing by showing the change in absolute simulation error relative to the observational data. It explicitly maps areas of improvement (demarcated in red) and degradation (in blue) in model performance when using PFT_{local} in place of PFT_{global}.

https://doi.org/10.5194/essd-2025-475
Preprint. Discussion started: 19 August 2025

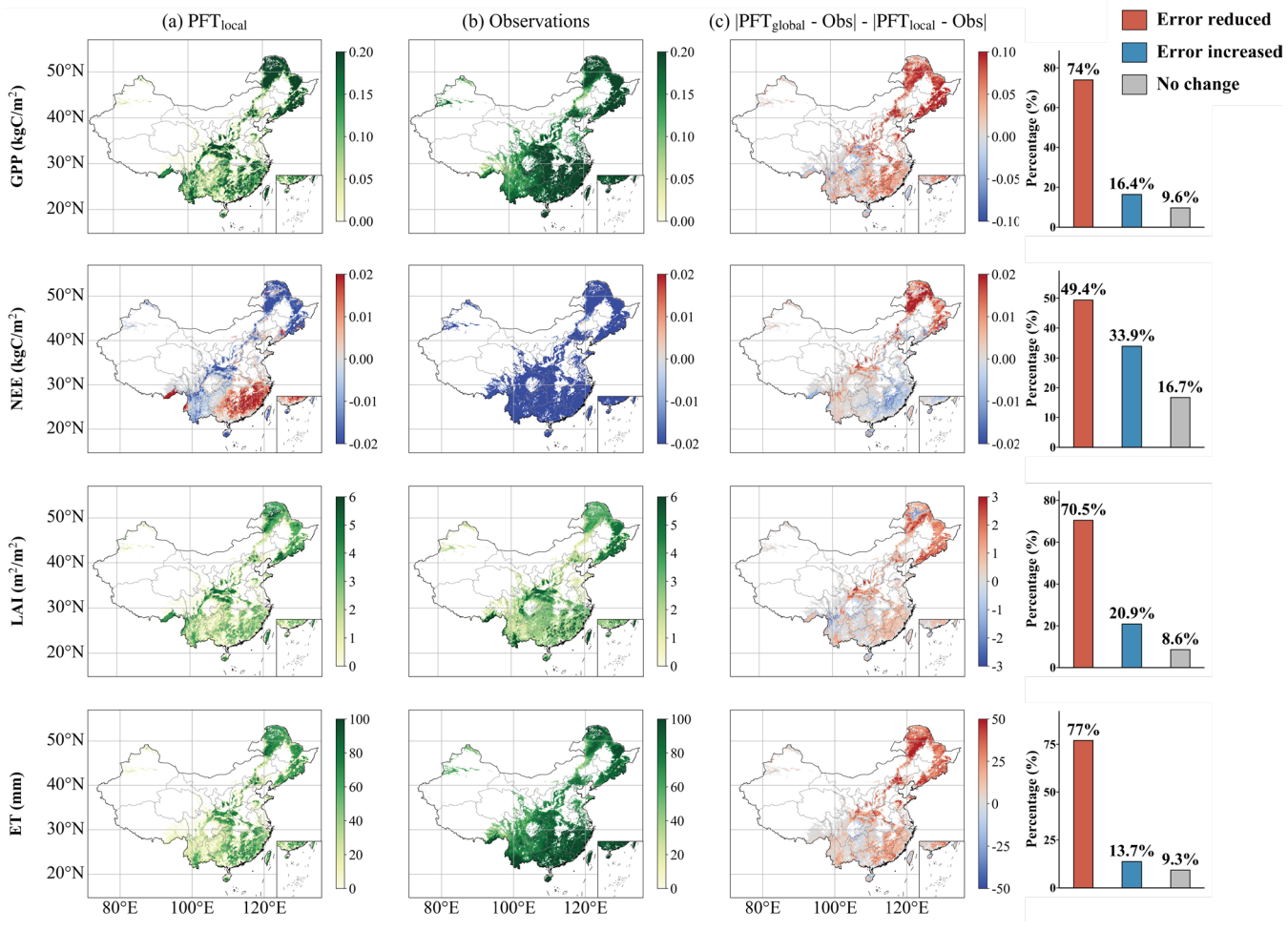

Figure 8. Model-data comparison for GPP, NEE, LAI, and ET for summer (June–August) 2010. **(a)** Ecosystem variables simulated by the LPJ–GUESS model using our reconstructed $\boldsymbol{PFT_{local}}$ dataset. **(b)** Corresponding observation-based benchmark products from FLUXCOM (GPP, NEE), GIMMS (LAI4g), and GLEAM (ET). **(c)** The difference in absolute error between model runs, calculated as $|\boldsymbol{PFT_{global} - Observation}| - |\boldsymbol{PFT_{local} - Observation}|$. Positive values indicate that $\boldsymbol{PFT_{local}}$ reduces the simulation error (improves performance) compared to $\boldsymbol{PFT_{global}}$, whereas negative values indicate an increase in error (performance degradation), and the right-hand bar graph displays the percentages of error reduced, increased, and no change.

High simulated GPP values (>0.2 kgC/m^2) are concentrated in the forested regions of northeastern (e.g., the Greater Khingan and Changbai Mountains), the central Qinling Mountains, and southeast China. Conversely, low GPP values are characteristic of the arid and semi-arid regions of the northwest and the Tibetan Plateau (Fig. 8a), where productivity is constrained by water availability and low temperatures. On a macroscale, the simulation accurately captures this geographical distribution. However, the model tends to underestimate GPP compared to the FLUXCOM product, particularly in northern, central, and southwestern China (Fig. 8a and 8b). Regarding the impact of the PFT forcing, the PFT_{local} map demonstrates a distinct advantage by reducing simulation errors across 74% of the domain, where it reduces simulation error (red areas in Fig. 8c). In other areas,

https://doi.org/10.5194/essd-2025-475
Preprint. Discussion started: 19 August 2025

such as southwestern and parts of central China, using PFT_{local} increases the simulation error compared to PFT_{global} (blue areas in Fig. 8c).

The simulation of NEE exhibits greater uncertainty compared to that of GPP. Observational data (Fig. 8b) indicate that China's forested regions function as strong carbon sinks during the summer (NEE < -0.02 kgC/m^2). While the PFT_{local} driven simulation correctly identifies northeastern, central, and southwestern China as carbon sinks, it incorrectly depicts eastern China, particularly the southeast, as a strong carbon source (NEE > 0.02 kgC/m^2), thus failing to reproduce the observed magnitude of carbon uptake in these forests (Fig. 8a). Despite this systematic bias, the use of PFT_{local} results in a substantial improvement of 49.4% in the simulation of NEE relative to PFT_{global} (Fig. 8c). Across large portions of the country, especially in the northeast, the absolute error is substantially reduced (indicated by deep red coloration). The areas where simulation error increases (blue regions) are concentrated in parts of eastern and southeastern China.

The simulated LAI exhibits a spatial pattern analogous to that of GPP, characterized by a general decline in values from east to west. However, when compared against the observation-based data, the model demonstrates an underestimate of LAI, particularly pronounced in southern China. The application of the PFT_{local} dataset substantially reduces LAI simulation errors across 70.5% of the domain (demarcated by red in Fig. 8c), underscoring the superiority of the new PFT map. Nevertheless, in some parts of the northeast and southwest, the LAI simulation error increases (blue areas), in strong spatial correspondence with the areas of increased GPP error.

The simulation of ET demonstrates a spatial pattern consistent with the other variables analyzed. In simulations driven by PFT_{local}, high ET values are concentrated in southeastern and northeastern China (Fig. 8a). Relative to remote sensing-derived products (Fig. 8b), the model exhibits a general underestimation of ET. In terms of model improvement (Fig. 8c), PFT_{local} substantially reduces the simulation error across 77% of China (indicated by large swaths of red), apart from some regions in the southwest.

5 Discussion

5.1 Comparison with other forest datasets

The spatial accuracy of the reconstructed PFT dataset was quantitatively evaluated against four existing products (MODIS, ESA CCI, CLCNMO, and GLC_FCS30). The assessment utilized 2,860 ground-truth samples of needleleaf and broadleaf forests from nationwide field surveys conducted from 2011–2013 (Fig. S6). For direct comparison, all datasets were standardized to a 1km resolution within the same projection and spatial extent. The reconstructed PFT dataset achieved an overall classification accuracy of 88.51%, which is higher than MODIS (68.74%), ESA CCI (86.46%), CLCNMO (77.46%), and GLC_FCS30 (86.52%) (Table 5). Specifically: For broadleaf forests, the dataset's accuracy (89.12%) surpassed most products, though it was slightly lower than GLC_FCS30 (90.12%). For needleleaf forests, the dataset's accuracy (87.91%) was the highest among all evaluated products. Although the User's Accuracy (UA) and Producer's Accuracy (PA) were not

https://doi.org/10.5194/essd-2025-475
Preprint. Discussion started: 19 August 2025

555 uniformly superior, the dataset's F1-score (87.91%) was highest. This independent validation confirms the high spatial accuracy of the reconstructed PFT data in comparison to prominent existing datasets.

Table 5. Comparison of mapping accuracy based on ground-truth samples from 2011–2013 for this study, MODIS, ESA CCI, CLCNMO, and GLC_FCS30.

		Broadleaf				Needleleaf				Overall
		2011	2012	2013	Mean	2011	2012	2013	Mean	Mean
This study	PA (%)	82.35	86.79	93.92	87.69	77.52	84.81	81.38	81.24	84.46
	UA (%)	87.32	92.4	91.89	90.54	90.24	93.18	95.93	93.12	91.83
	F1 (%)	84.76	89.51	92.9	89.06	83.4	88.8	88.06	86.75	87.91
	OA (%)	85.41	89.93	92.02	89.12	84.35	89.19	90.18	87.91	88.51
MODIS	PA (%)	62.55	64.82	69.06	65.48	14.48	19.42	14.48	16.13	40.80
	UA (%)	90.37	92.68	88.65	90.57	96.2	92.45	91.3	93.32	91.94
	F1 (%)	73.93	76.29	77.64	75.95	25.17	32.1	25	27.42	51.69
	OA (%)	78.26	80.05	77.91	78.74	56.33	58.51	61.35	58.73	68.74
ESA_CCI	PA (%)	80	86.12	91.71	85.94	73.33	76.09	73.1	74.17	80.06
	UA (%)	89.28	92.21	91.21	90.90	91.02	92.75	92.98	92.25	91.58
	F1 (%)	84.38	89.06	91.46	88.30	81.22	83.6	81.85	82.22	85.26
	OA (%)	85.41	89.53	90.49	88.48	82.8	84.92	85.58	84.43	86.46
CLCNMO[a]	PA (%)	-	-	90.61	90.61	-	-	33.1	33.1	61.86
	UA (%)	-	-	83.25	83.25	-	-	100	100	91.63
	F1 (%)	-	-	86.77	86.77	-	-	49.74	49.74	68.26
	OA (%)	-	-	84.66	84.66	-	-	70.25	70.25	77.46
GLC_FCS30[b]	PA (%)	87.25	-	96.13	91.69	68.57	-	64.14	66.36	79.02
	UA (%)	88.65	-	90.16	89.41	95.49	-	97.89	96.69	93.05
	F1 (%)	87.94	-	93.05	90.50	79.82	-	77.5	78.66	84.58
	OA (%)	88.21	-	92.02	90.12	82.42	-	83.44	82.93	86.52

Notes: PA, UA and OA are abbreviations for the producer's accuracy, user's accuracy, and overall accuracy, respectively. The
560 F1 represents the harmonic mean of the PA and the UA.
[a.] The CLCNMO dataset was only available for 2013.
[b.] The GLC_FCS30 dataset is produced at 5-year intervals. For this study's validation, its 2010 data was used as a proxy for 2011, and its 2015 data was used as a proxy for 2013.

The temporal evolution of the reconstructed PFT dataset aligns closely with NFI records, which document a significant
565 increase in national forest cover from approximately 12% in the early 1980s to 24% at present, largely due to extensive afforestation programs (Fig. 5). In contrast, existing LULC products overwhelmingly fail to reproduce the historical trend of forest expansion in China since the 1980s (Fig. 5). Nearly all these datasets substantially underestimate the rate of forest growth. The CNLUCC dataset, for example, depicts a largely static forest area from 1980 to 2023, thereby failing to capture the marked gains resulting from China's afforestation programmes. Although the GLASS_GLC product indicates an increase, its forest

https://doi.org/10.5194/essd-2025-475
Preprint. Discussion started: 19 August 2025

area estimations are considerably higher than the official NFI statistics. Moreover, existing LULC products are unable to accurately resolve the divergent historical trajectories of needleleaf and broadleaf forests. Therefore, a re-evaluation of the impacts of China's forest cover change on terrestrial ecosystems using this newly developed, validated dataset is warranted.

5.2 A spatiotemporally constrained approach for reconstructing forest PFTs via multi-source data fusion

This study developed a method to integrate the "top-down" spatial detail derived from multi-source remote sensing products with the "bottom-up" statistical constraints provided by the NFI. The methodology involved harmonizing disparate LULC data sources into a uniform spatial framework via systematic resampling, re-projection, and aggregation. A consistency metric (CON) was computed to quantitatively assess spatial disagreements in forest identification among these sources. This metric functions as a diagnostic tool, elucidating inter-source congruence and leveraging this consensus to construct more robust maps of forest cover and PFTs; pixels with higher CON values are prioritized, whereas regions with low CON values, indicative of poor source data consensus, are assigned a lower priority unless their inclusion is mandated by NFI area constraints. This strategy effectively mitigates classification-level uncertainty by integrating a "majority vote" consensus with external statistical controls. Furthermore, the approach utilizes an annual maximum NDVI mask to delineate supplementary forest patches. This application of an NDVI mask, supported by prior research, effectively filters spurious forest signals from mountainous terrains, barren lands, and sparsely vegetated areas (Qin et al., 2015).

Therefore, our methodology addresses the intrinsic limitations of relying on a single data modality, resolving a well-documented deficiency in extant land cover products. Specifically, these products often fail to represent the full extent of the significant, policy-driven expansion of Chinese forests post-1980, thereby underestimating the rate of forest cover growth (Fig. 5) (Yue et al., 2024; Zhu et al., 2025; Yu et al., 2022). Consequently, DGVMs driven by these historically inaccurate datasets are likely to substantially underestimate China's carbon sink. We tested the hypothesis that a more accurate vegetation map would improve land surface model performance. Driving the LPJ–GUESS dynamic vegetation model with our reconstructed PFT maps resulted in markedly improved simulations compared to those using the ESA CCI global PFT dataset (Fig. 8 and Fig. S10). The spatial pattern of these improvements aligns directly with regions where our dataset's tree cover diverges most from the global product, especially in northeastern China (Fig. 7 and Fig. S9). This provides powerful evidence for the critical role of accurate vegetation representation in simulating carbon and water cycles. By providing a more precise depiction of historical forest dynamics, our dataset offers stronger constraints on model parameterizations of surface albedo, canopy structure, and transpiration, leading to more robust flux estimations.

5.3 Limitations and future work

First, as an integrated data product, our dataset inherits uncertainties from its primary sources: the input LULC data and the NFI statistics. Most satellite based LULC datasets rely on machine learning classifiers, whose accuracy is contingent upon the representativeness, quantity, and quality of training samples. Furthermore, our dataset's accuracy is substantially dependent on the NFI data, which possesses its own uncertainties stemming from inventory methodologies and the representativeness of

https://doi.org/10.5194/essd-2025-475
Preprint. Discussion started: 19 August 2025

ground plots. Notably, the precision of NFI data has improved over time due to the progressive evolution of its sampling design; for example, the introduction of combined ground-truth and remote sensing samples in the fourth NFI (1989–1993) and a significant increase in remote sensing samples since the sixth NFI (1999–2003) markedly enhanced its accuracy (Lei et al., 2009). Consequently, any uncertainty within the NFI data will inevitably propagate into our reconstructed dataset.

Second, for provinces with limited historical data (e.g., Chongqing, Hong Kong, and Macau), we employed linear extrapolation to generate annual provincial-level statistics. This approach was predicated on prior findings that national afforestation targets exhibit a quasi-linear temporal trend (an increase of ~1.8 million ha/year) (He et al., 2024; Xu et al., 2023), suggesting a consistent, progressive afforestation strategy driven by government policy. Nevertheless, this method introduces a degree of uncertainty (Fig. S1). To mitigate this, we constrained the extrapolated area by defining a consistency-level threshold, which was selected to ensure that the cumulative area of all pixels at or above this level most closely matched the target value for a given year. While this technique maximizes spatial and quantitative accuracy under the available data constraints, discrepancies may still exist between our reconstructed results and the actual forest area in these provinces prior to 2003, where the true conditions are unknown.

Finally, while our PFT distribution map significantly improves the simulation performance of DGVMs compared to the ESA CCI PFT product, this model-based validation is relative, not absolute. This can lead to discrepancies between simulated outcomes and on-the-ground reality (Fig. 8a, b, Fig. S10a, b), with errors potentially attributable to the internal parameterization of the LPJ–GUESS model. The model's default parameters are primarily calibrated for European ecosystems and may not align with the unique ecophysiology, disturbance regimes, and soil hydrology of China (Li et al., 2022; Peng et al., 2019). A comprehensive, large-scale parameter calibration for China was beyond the scope of this study. A key avenue for future research is to disentangle the interacting uncertainties among data inputs, model structure, and climate drivers. Enhancing differentiated, regional-scale modeling and identifying underlying mechanisms will be critical for improving the predictive power of terrestrial ecosystem models and the accuracy of forest carbon sink estimations in China.

6 Data availability

The reconstructed forest cover dataset generated in this study is publicly available in the Zenodo repository at https://doi.org/10.5281/zenodo.16208012 (Liu et al., 2025). All third-party datasets used for this analysis are publicly available from their original sources as listed below: National Forest Inventory records for China are accessible from the National Forestry and Grassland Data Center at http://www.forestdata.cn/. The following datasets are available from the Resource and Environment Science and Data Center (https://www.resdc.cn/): the China National Land Use/Cover Change (CNLUCC), Moderate Resolution Land Use and Cover (MLUD), and Wu_LC datasets (last access: 7 May 2025). The following datasets were accessed via Google Earth Engine (https://code.earthengine.google.com): the Copernicus Global Land Service (CGLS), MODIS Land Cover Type (MCD12Q1), Hansen Global Forest Change (Hansen), JRC Forest Types, and Global Forest Canopy Height (GFCH) (last access: 13 April 2025). The following datasets are provided by the European Space Agency (ESA)

https://doi.org/10.5194/essd-2025-475
Preprint. Discussion started: 19 August 2025

(http://climate.esa.int/en/projects/land-cover): ESACCI_LC, GlobCover, and ESA_WorldCover (last access: 12 April 2025). Datasets from Tsinghua University (http://data.ess.tsinghua.edu.cn), including FROM_GLC, GLASS_GLC, and the first all-season sample set for mapping global land cover with Landsat-8 data, were accessed from their data portal (last access: 10 April 2025). China Land Cover Dataset (CLCD) is publicly available at https://doi.org/10.5281/zenodo.4417810 (Yang and Huang, 2021). Global Land-Cover-Related Datasets with Fine Classification System (GLC_FCS30) is publicly available at https://doi.org/10.5281/zenodo.8239305 (Liu et al., 2023). Global Forest Cover 30m (GFC30) is available from the Data Sharing and Service Portal at https://data.casearth.cn/dataset/6188d5be819aec0dc5853a4d (last access: 10 April 2025). Global Land Cover 2000 (GLC2000) is available from the National Earth System Science Data Center at https://www.geodata.cn/data/datadetails.html?dataguid=60781990406898&docId=12324 (last access: 10 April 2025). Consensus Land Cover of northern mid-to-high latitudes (CLCNMO) is publicly available at https://globalmaps.github.io/glcnmo.html (last access: 12 April 2025). GlobeLand30 is available for download from the National Geomatics Center of China at http://www.globallandcover.com/ (last access: 10 April 2025). Long-term Normalized Difference Vegetation Index (Jeong's NDVI) is available from Seoul National University at https://www.environment.snu.ac.kr/data/long-term-vi (last access: 11 April 2025). The Köppen–Geiger climate classification maps are available from Figshare at https://figshare.com/articles/dataset/Present_and_future_K_ppen-Geiger_climate_classification_maps_at_1-km_resolution/6396959/2 (last access: 26 May 2025). A global topographic dataset is publicly available from Earthenv at https://www.earthenv.org/topography (last access: 25 May 2025). ERA5-Land monthly averaged data (2m temperature, total precipitation, surface solar radiation downwards) are publicly available from the Copernicus Climate Data Store at https://cds.climate.copernicus.eu/datasets/reanalysis-era5-land-monthly-means?tab=overview (last access: 21 September 2024). Fluxcom GPP and NEE products are available from the project website at https://fluxcom.org/CF-Products/ (last access: 10 January 2025). GIMMS LAI4g is publicly available in the Zenodo repository at https://doi.org/10.5281/zenodo.7649107 (Cao et al., 2023). GLEAM Evapotranspiration (ET) products are available for download at https://www.gleam.eu/#downloads (last access: 23 July 2024).

7 Conclusion

To address the failure of existing land cover products in capturing the extensive forest expansion from large-scale afforestation in China since 1980, this study presents a reconstructed dataset of annual forest cover at 1 km resolution for the period 1980–2023 and the distribution of eight PFTs from 1981–2013. This paper details a method that integrates spatial forest distribution constraints from a suite of remote sensing products with provincial-level forest area constraints from NFI. The resultant dataset reproduces NFI-consistent forest dynamics with a 95.3% overall accuracy ($R^2 \approx 1$), and its application within a DGVM markedly improves the simulation accuracy of key ecosystem variables by 49.4% to 77%. This work thus provides a critical data foundation for more robust assessments of the ecological effects of forest restoration and for refining regional carbon sink estimations. The dataset's reliability is, however, inherently constrained by uncertainties in the source data, particularly in

https://doi.org/10.5194/essd-2025-475
Preprint. Discussion started: 19 August 2025

highly fragmented landscapes. Future research should therefore aim to decouple the interplay between data inputs, model structure, and climate drivers to advance the predictive capability of ecosystem models further.

Author contributions

Conceptualization, Bo.L., Boy.L., J.L., and Q.F.; Data curation, Bo.L.; Formal analysis, Bo.L.; Investigation, Bo.L., F.F., and Y.B.; Methodology, Bo.L.; Supervision, Boy.L., J.L., and Q.F.; Validation, Bo.L., F.F., and Y.B.; Visualization, Bo.L. and Y.B.; Writing (original draft preparation), Bo.L.; Writing (review and editing), Boy.L. All authors have read and agreed to the published version of the manuscript.

Competing interests

The authors declare that they have no conflict of interest.

Acknowledgements

The authors greatly appreciate the numerous organizations that made their data publicly available for this research. We sincerely thank the ESA for providing the ESACCI_LC, GlobCover, and ESA_WorldCover products; and the National Aeronautics and Space Administration (NASA) for the MCD12Q1 product. We acknowledge the data providers in China, including: the National Forestry and Grassland Data Center for the national forest inventory records; the Resource and Environment Science and Data Center (RESDC) for the CNLUCC, MLUD, and Wu_LC datasets; the National Geomatics Center of China for the GlobeLand30 dataset; the Data Sharing and Service Portal for the GFC30 dataset; and the National Earth System Science Data Center for the GLC2000 dataset. We also extend special thanks to Tsinghua University for providing the FROM_GLC and GLASS_GLC datasets, as well as the first all-season sample set for mapping global land cover with Landsat-8 data. We also extend our thanks to the University of Maryland for the Hansen Global Forest Change dataset; the Joint Research Centre of the European Commission for the JRC Forest Types dataset; Seoul National University for the Jeong's NDVI data; the Copernicus Climate Data Store for the ERA5–Land reanalysis data; the Earthenv repository for the global topographic dataset; and the providers of the FLUXCOM, GIMMS and GLEAM products. Finally, we offer our sincere gratitude to the developers of the LPJ–GUESS model for providing a valuable simulation tool, and to the Google Earth Engine team for developing and maintaining their powerful, planetary-scale platform for geospatial analysis. We also wish to acknowledge the AI model, Gemini 2.5 Pro, for its assistance in improving the language and style of the manuscript and in editing and inserting references.

https://doi.org/10.5194/essd-2025-475
Preprint. Discussion started: 19 August 2025

Financial support

This research was supported by the National Natural Science Foundation of China (grant no. 42371101), the Young Science and Technology New Star Project of Shaanxi Province (grant no. 2024ZC-KJXX-013), the Qin Chuangyuan Cites High-level Innovation or Entrepreneurship Talent Project (grant no. QCYRCXM-2023-066), the fifth batch special funding (Pre-Station) from China Postdoctoral Science Foundation (grant no. 2023TQ0207), and the Fundamental Research Funds for the Central Universities (grant nos. GK202304024, 1110011297, 1112010355).

References

Alkama, R., and Cescatti, A.: Biophysical climate impacts of recent changes in global forest cover, *Science*, 351, 600–604, https://doi.org/10.1126/science.aac8083, 2016.

Amatulli, G., Domisch, S., Tuanmu, M.-N., Parmentier, B., Ranipeta, A., Malczyk, J., and Jetz, W.: A suite of global, cross-scale topographic variables for environmental and biodiversity modeling, *Sci. Data*, 5, 1–15, https://doi.org/10.1038/sdata.2018.40, 2018.

Beck, H. E., Zimmermann, N. E., McVicar, T. R., Vergopolan, N., Berg, A., and Wood, E. F.: Present and future Köppen-Geiger climate classification maps at 1-km resolution, *Sci. Data*, 5, 1–12, https://doi.org/10.1038/sdata.2018.214, 2018.

Bergkvist, J., Lagergren, F., Islam, M. R., Wårlind, D., Miller, P. A., Finnander Linderson, M. L., Lindeskog, M., and Jönsson, A. M.: Quantifying the impact of climate change and forest management on Swedish forest ecosystems using the dynamic vegetation model LPJ-GUESS, *Earths Future*, 13, e2024EF004662, https://doi.org/10.1029/2024EF004662, 2025.

Bonan, G. B., Levis, S., Kergoat, L., and Oleson, K. W.: Landscapes as patches of plant functional types: An integrating concept for climate and ecosystem models, *Global Biogeochem. Cy.*, 16, 5-1, https://doi.org/10.1029/2000GB001359, 2002.

Cao, S., Li, M., Zhu, Z., Wang, Z., Zha, J., Zhao, W., Duanmu, Z., Chen, J., Zheng, Y., Chen, Y., Myneni, R. B., and Piao, S.: Spatiotemporally consistent global dataset of the GIMMS Leaf Area Index (GIMMS LAI4g) from 1982 to 2020 (V1.2). Zenodo [data], https://doi.org/10.5281/zenodo.7649107, 2023.

Chen, C., Park, T., Wang, X., Piao, S., Xu, B., Chaturvedi, R. K., Fuchs, R., Brovkin, V., Ciais, P., and Fensholt, R.: China and India lead in greening of the world through land-use management, *Nat. Sustain.*, 2, 122–129, https://doi.org/10.1038/s41893-019-0220-7, 2019.

Chen, J., Chen, J., Liao, A., Cao, X., Chen, L., Chen, X., He, C., Han, G., Peng, S., and Lu, M.: Global land cover mapping at 30 m resolution: A POK-based operational approach, *ISPRS J. Photogramm. Remote Sens.*, 103, 7–27, https://doi.org/10.1016/j.isprsjprs.2014.09.002, 2015.

Fang, J., Chen, A., Peng, C., Zhao, S., and Ci, L.: Changes in forest biomass carbon storage in China between 1949 and 1998, *Science*, 292, 2320–2322, https://doi.org/10.1126/science.1058629, 2001.

Fang, X., Zhao, W., Zhang, C., Zhang, D., Wei, X., Qiu, W., and Ye, Y.: Methodology for credibility assessment of historical global LUCC datasets, *Sci. China Earth Sci.*, 63, 1013–1025, https://doi.org/10.1007/s11430-019-9592-y, 2020.

https://doi.org/10.5194/essd-2025-475
Preprint. Discussion started: 19 August 2025

Food and Agriculture Organization of the United Nations. State of the world's forests 2016. Forests and agriculture: Land-use challenges and opportunities. FAO Report, 2016.

Friedlingstein, P., O'Sullivan, M., Jones, M. W., Andrew, R. M., Hauck, J., Landschützer, P., Le Quéré, C., Li, H., Luijkx, I. T., and Olsen, A.: Global carbon budget 2024, *Earth Syst. Sci. Data*, 17, 965–1039, https://doi.org/10.5194/essd-2024-519, 2025.

Ge, Q., Dai, J., He, F., Pan, Y., and Wang, M.: Land use changes and their relations with carbon cycles over the past 300 a in China, *Sci. China Ser. D Earth Sci.*, 51, 871–884, https://doi.org/10.1007/s11430-008-0067-8, 2008.

Gregor, K., Reyer, C. P., Nagel, T. A., Mäkelä, A., Krause, A., Knoke, T., and Rammig, A.: Reconciling the EU forest, biodiversity, and climate strategies, *Global Change Biol.*, 30, e17431, https://doi.org/10.1111/gcb.17431, 2024.

Hansen, M. C., Potapov, P. V., Moore, R., Hancher, M., Turubanova, S. A., Tyukavina, A., Thau, D., Stehman, S. V., Goetz, S. J., and Loveland, T. R.: High-resolution global maps of 21st-century forest cover change, *Science*, 342, 850–853, https://doi.org/10.1126/science.1244693, 2013.

Harper, K. L., Lamarche, C., Hartley, A., Peylin, P., Ottlé, C., Bastrikov, V., San Martín, R., Bohnenstengel, S. I., Kirches, G., and Boettcher, M.: A 29-year time series of annual 300 m resolution plant-functional-type maps for climate models, *Earth Syst. Sci. Data*, 15, 1465–1499, https://doi.org/10.5194/essd-15-1465-2023, 2023.

Hartung, K., Bastos, A., Chini, L., Ganzenmüller, R., Havermann, F., Hurtt, G. C., Loughran, T., Nabel, J. E. M. S., Nützel, T., and Obermeier, W. A.: Bookkeeping estimates of the net land-use change flux–a sensitivity study with the CMIP6 land-use dataset, *Earth Syst. Sci. Data*, 12, 763–782, https://doi.org/10.5194/essd-12-763-2021, 2021.

He, Y., Piao, S., Ciais, P., Xu, H., and Gasser, T.: Future land carbon removals in China consistent with national inventory, *Nat. Commun.*, 15, 10426, https://doi.org/10.1038/s41467-024-54846-2, 2024.

Hong, S., Yin, G., Piao, S., Dybzinski, R., Cong, N., Li, X., Wang, K., Peñuelas, J., Zeng, H., and Chen, A.: Divergent responses of soil organic carbon to afforestation, *Natl. Sci. Rev.*, 3, 694–700, https://doi.org/10.1093/nsr/nwz203, 2020.

Houghton, R. A., and Hackler, J. L.: Sources and sinks of carbon from land-use change in China, *Global Biogeochem. Cy.*, 17, 1034, https://doi.org/10.1029/2002GB001970, 2003.

Industry Development Sub-center, Statistical Table of Main Indicators of Forest Resources by Province (Autonomous Region, Municipality) in the Ninth National Class I Forest Inventory, National Forestry and Grassland Scientific Data Center, 2018, CSTR:17575.11.0120230320014.0018.V1.

Islam, M. R., Jönsson, A. M., Bergkvist, J., Lagergren, F., Lindeskog, M., Mölder, M., Scholze, M., and Kljun, N.: Projected effects of climate change and forest management on carbon fluxes and biomass of a boreal forest, *Agric. For. Meteorol.*, 349, 109959, https://doi.org/10.1016/j.agrformet.2024.109959, 2024.

Jeong, S., Ryu, Y., Gentine, P., Lian, X., Fang, J., Li, X., Dechant, B., Kong, J., Choi, W., and Jiang, C.: Persistent global greening over the last four decades using novel long-term vegetation index data with enhanced temporal consistency, *Remote Sens. Environ.*, 311, 114282, https://doi.org/10.1016/j.rse.2024.114282, 2024.

https://doi.org/10.5194/essd-2025-475
Preprint. Discussion started: 19 August 2025

Lei, X., Tang, M., Lu, Y., Hong, L., and Tian, D.: Forest inventory in China: status and challenges, *Int. Forest. Rev.*, 11, 52–63, https://doi.org/10.1505/ifor.11.1.52, 2009.

Li, C., Gong, P., Wang, J., Zhu, Z., Biging, G. S., Yuan, C., Hu, T., Zhang, H., Wang, Q., and Li, X.: The first all-season sample set for mapping global land cover with Landsat-8 data, *Sci. Bull.*, 62, 508–515, https://doi.org/10.1016/j.scib.2017.03.011, 2017.

Li, X., Zhang, H., Shang, R., Chen, J., Wang, D., Zhu, J., Huang, H., Lin, S., Pan, B., and Yuan, W.: It is time to optimize forest management policy for both carbon sinks and wood harvest in China, *Natl. Sci. Rev.*, 12, nwae464, https://doi.org/10.1093/nsr/nwae464, 2025.

Li, Y., Wang, Y., Sun, Y., and Li, J.: Global sensitivity analysis of the LPJ model for larix olgensis Henry forests NPP in Jilin Province, China, *Forests*, 13, 874, https://doi.org/10.3390/f13060874, 2022.

Lindeskog, M., Lagergren, F., Smith, B., and Rammig, A.: Accounting for forest management in the estimation of forest carbon balance using the dynamic vegetation model LPJ-GUESS (v4. 0, r9333): Implementation and evaluation of simulations for Europe, *Geosci. Model Dev.*, 14, 5887–5925, https://doi.org/10.5194/gmd-14-5887-2021, 2021.

Liu, B., Li, B., Feng, F., Bao, Y., Li, J., and Feng, Q.: 1 km annual forest cover and plant functional types dataset for China from 1980 to 2023. Zenodo [data], https://doi.org/10.5281/zenodo.16208012, 2025.

Liu, L., Zhang, X., and Zhao T.: GLC_FCS30D: the first global 30-m land-cover dynamic monitoring product with fine classification system from 1985 to 2022, Zenodo [data], https://doi.org/10.5281/zenodo.8239305, 2023.

Liu, S., Bond-Lamberty, B., Boysen, L. R., Ford, J. D., Fox, A., Gallo, K., Hatfield, J., Henebry, G. M., Huntington, T. G., and Liu, Z.: Grand challenges in understanding the interplay of climate and land changes, *Environ. Int.*, 21, 1–43, https://doi.org/10.1016/j.envint.2016.09.007, 2017.

O'Sullivan, M., Friedlingstein, P., Sitch, S., Anthoni, P., Arneth, A., Arora, V. K., Bastrikov, V., Delire, C., Goll, D. S., and Jain, A. K.: Process-oriented analysis of dominant sources of uncertainty in the land carbon sink, *Nat. Commun.*, 13, 4781, https://doi.org/10.1038/s41467-022-32416-8, 2022.

Peng, S., Terrer, C., Smith, B., Ciais, P., Han, Q., Nan, J., Fisher, J. B., Chen, L., Deng, L., and Yu, K.: Carbon restoration potential on global land under water resource constraints, *Nat. Water*, 2, 1071–1081, https://doi.org/10.1038/s44221-024-00295-6, 2024a.

Peng, S., Yu, K., Li, Z., Wen, Z., and Zhang, C.: Integrating potential natural vegetation and habitat suitability into revegetation programs for sustainable ecosystems under future climate change, *Agric. For. Meteorol.*, 269, 270–284, https://doi.org/10.1016/j.agrformet.2019.02.023, 2019.

Peng, X., He, G., Wang, G., Yin, R., Yang, R., Peng, Y., Long, T., Zhang, Z., Chen, Y., and Wang, J.: GF-1 WFV satellite images based forest cover mapping in China supported by open land use/cover datasets, *Sci. Data*, 11, 1355, https://doi.org/10.1038/s41597-024-03774-z, 2024b.

Piao, S., Fang, J., Ciais, P., Peylin, P., Huang, Y., Sitch, S., and Wang, T.: The carbon balance of terrestrial ecosystems in China, *Nature*, 458, 1009–1013, https://doi.org/10.1038/nature07944, 2009.

https://doi.org/10.5194/essd-2025-475
Preprint. Discussion started: 19 August 2025

Piao, S., Wang, X., Park, T., Chen, C., Lian, X., He, Y., Bjerke, J. W., Chen, A., Ciais, P., and Tømmervik, H.: Characteristics, drivers and feedbacks of global greening, *Nat. Rev. Earth Environ.*, 1, 14–27, https://doi.org/10.1038/s43017-019-0001-x, 2020.

Pugh, T. A. M., Seidl, R., Liu, D., Lindeskog, M., Chini, L. P., and Senf, C.: The anthropogenic imprint on temperate and boreal forest demography and carbon turnover, *Global Ecol. Biogeogr.*, 33, 100–115, https://doi.org/10.1111/geb.13773, 2024.

Qin, Y., Xiao, X., Dong, J., Zhang, G., Shimada, M., Liu, J., Li, C., Kou, W., and Moore III, B.: Forest cover maps of China in 2010 from multiple approaches and data sources: PALSAR, Landsat, MODIS, FRA, and NFI, *ISPRS J. Photogramm. Remote Sens.*, 109, 1–16, https://doi.org/10.1016/j.isprsjprs.2015.08.008, 2015.

Ran, Y., Li, X., Lu, L., and Li, Z.: Large-scale land cover mapping with the integration of multi-source information based on the Dempster–Shafer theory, *Int. J. Geogr. Inf. Sci.*, 26, 169–191, https://doi.org/10.1080/13658816.2011.586181, 2012.

Ruehr, S., Keenan, T. F., Williams, C., Zhou, Y., Lu, X., Bastos, A., Canadell, J. G., Prentice, I. C., Sitch, S., and Terrer, C.: Evidence and attribution of the enhanced land carbon sink, *Nat. Rev. Earth Environ.*, 4, 518–534, https://doi.org/10.1038/s43017-023-00456-3, 2023.

Tong, X., Brandt, M., Yue, Y., Horion, S., Wang, K., De Keersmaecker, W., Tian, F., Schurgers, G., Xiao, X., and Luo, Y.: Increased vegetation growth and carbon stock in China karst via ecological engineering, *Nat. Sustain.*, 1, 44–50, https://doi.org/10.1038/s41893-017-0004-x, 2018.

Tu, Y., Wu, S., Chen, B., Weng, Q., Bai, Y., Yang, J., Yu, L., and Xu, B.: A 30 m annual cropland dataset of China from 1986 to 2021, *Earth Syst. Sci. Data*, 16, 2297–2316, https://doi.org/10.5194/essd-16-2297-2024, 2024.

Wei, X., Liu, R., Liu, Y., He, J., Chen, J., Qi, L., Zhou, Y., Qin, Y., Wu, C., and Dong, J.: Forest areas in China are recovering since the 21st century, *Geophys. Res. Lett.*, 51, e2024GL110312, https://doi.org/10.1029/2024GL110312, 2024.

Winkler, K., Fuchs, R., Rounsevell, M., and Herold, M.: Global land use changes are four times greater than previously estimated, *Nat. Commun.*, 12, 2501, https://doi.org/10.1038/s41467-021-22702-2, 2021.

Xia, X., Xia, J., Chen, X., Fan, L., Liu, S., Qin, Y., Qin, Z., Xiao, X., Xu, W., and Yue, C.: Reconstructing long-term forest cover in China by fusing national forest inventory and 20 land use and land cover data sets, *J. Geophys. Res.-Biogeo.*, 128, e2022JG007101, https://doi.org/10.1029/2022JG007101, 2023.

Xu, H., Yue, C., Zhang, Y., Liu, D., and Piao, S.: Forestation at the right time with the right species can generate persistent carbon benefits in China, *Proc. Natl. Acad. Sci. USA*, 120, e2304988120, https://doi.org/10.1073/pnas.2304988120, 2023.

Yang, D., and Song, W.: Tracking land use trajectory to map abandoned farmland in mountainous area, *Environ. Int.*, 75, 102103, https://doi.org/10.1016/j.envint.2022.102103, 2023.

Yang, H., Wang, S., Son, R., Lee, H., Benson, V., Zhang, W., Zhang, Y., Zhang, Y., Kattge, J., and Boenisch, G.: Global patterns of tree wood density, *Global Change Biol.*, 30, e17224, https://doi.org/10.1111/gcb.17224, 2024.

Yang, J., and Huang, X.: 30 m annual land cover and its dynamics in China from 1990 to 2019, *Earth Syst. Sci. Data*, 13, 2021–2039, https://doi.org/10.5194/essd-13-2021, 2021.

https://doi.org/10.5194/essd-2025-475
Preprint. Discussion started: 19 August 2025

Yang, J. and Huang, X.: 30m annual land cover and its dynamics in China from 1990 to 2019, Zenodo [data], https://doi.org/10.5281/zenodo.4417810, 2021.

Yu, Z., Ciais, P., Piao, S., Houghton, R. A., Lu, C., Tian, H., Agathokleous, E., Kattel, G. R., Sitch, S., and Goll, D.: Forest expansion dominates China's land carbon sink since 1980, *Nat. Commun.*, 13, 5374, https://doi.org/10.1038/s41467-022-32909-y, 2022.

Yu, Z., Liu, S., Li, H., Liang, J., Liu, W., Piao, S., Tian, H., Zhou, G., Lu, C., and You, W.: Maximizing carbon sequestration potential in Chinese forests through optimal management, *Nat. Commun.*, 15, 3154, https://doi.org/10.1038/s41467-024-47143-5, 2024.

Yue, C., Xu, M., Ciais, P., Tao, S., Shen, H., Chang, J., Li, W., Deng, L., He, J., and Leng, Y.: Contributions of ecological restoration policies to China's land carbon balance, *Nat. Commun.*, 15, 9708, https://doi.org/10.1038/s41467-024-54019-3, 2024.

Zeng, W., Tomppo, E., Healey, S. P., and Gadow, K. V.: The national forest inventory in China: history-results-international context, *For. Ecosyst.*, 2, 23, https://doi.org/10.1186/s40663-015-0047-1, 2015.

Zhu, Y., Xia, X., Canadell, J. G., Piao, S., Lu, X., Mishra, U., Wang, X., Yuan, W., and Qin, Z.: China's carbon sinks from land-use change underestimated, *Nat. Clim. Change*, 15, 428–435, https://doi.org/10.1038/s41558-024-02167-y, 2025.